JOURNAL OF MATERIALS RESEARCH AND TECHNOLOGY 2022;18:1391–1411

Available online at www.sciencedirect.com

jmr&t Journal of Materials Research and Technology

journal homepage: www.elsevier.com/locate/jmrt

Original Article

Multi-objective optimisation for mortar containing activated waste glass powder

Junbo Sun [a], *Long Yue* [b], *Kai Xu* [b], *Rui He* [b], *Xupei Yao* [c], *Mengcheng Chen* [d], *Tong Cai* [e], *Xiangyu Wang* [f,*], *Yufei Wang* [f,**]

[a] *Institute for Smart City of Chongqing University in Liyang, Chongqing University, Jiangsu, 213300, China*
[b] *School of Architectural Engineering, Nanjing Institute of Technology, Nanjing 211167, China*
[c] *Department of Civil Engineering, Monash University, Clayton, Victoria, 3800, Australia*
[d] *School of Civil Engineering and Architecture, East China Jiao Tong University, Nanchang 330013, China*
[e] *School of Civil, Environmental and Mining Engineering, The University of Western Australia, Crawley, WA 6009, Australia*
[f] *School of Design and Built Environment, Curtin University, Perth, WA 6102, Australia*

ARTICLE INFO

Article history:
Received 16 December 2021
Accepted 24 February 2022
Available online 3 March 2022

Keywords:
Waste glass powder
Activation methodology
Multi-objective optimisation
Machine learning
Unconfined compressive strength
Alkali-silica reaction

ABSTRACT

Waste glass is inert and non-degradable which leads to enormous environmental and sustainability troubles, but it can be reused in concrete due to the potential of the pozzolanic activity. This study proposes methods on activity excitation of waste glass powder (WGP) including mechanical, chemical, and mechanical-chemical activation. The results showed that the mortar containing 30% 75 μm WGP activated by the mechanical-chemical method was optimal to increase the mechanical property and reduce the detrimental expansion. In addition, the microstructural analysis was conducted to explore the activation effect on WGP and WGP-cement system. An artificial intelligence (AI) based multi-objective optimisation (MOO) model was proposed to seek the optimal mix proportions for the unconfined compression strength (UCS), alkali-silica reaction (ASR), and cost. A comprehensive dataset was investigated including 549 specimens for the UCS test and 366 test results for the expansion test. Random Forest (RF) model was utilized for the prediction of UCS and ASR values with hyperparameters tuned by a firefly algorithm (FA). The high correlation coefficients (0.93 for UCS and 0.91 for ASR) verified the feasibility of FA-RF. Subsequently, the FA-RF model was extended as the objective function for the multi-objective firefly algorithm (MOFA-RF) to obtain the consequent Pareto fronts. This paper combined the results of experiments, machine learning prediction, and multi-objective optimisation design for activated WGP mortar, which provided a comprehensive basis for the practical application.

© 2022 The Authors. Published by Elsevier B.V. This is an open access article under the CC BY-NC-ND license (http://creativecommons.org/licenses/by-nc-nd/4.0/).

* Corresponding author.
** Corresponding author.
E-mail addresses: Xiangyu.Wang@curtin.edu.au (X. Wang), wangyf0113_suz@163.com (Y. Wang).

https://doi.org/10.1016/j.jmrt.2022.02.123

2238-7854/© 2022 The Authors. Published by Elsevier B.V. This is an open access article under the CC BY-NC-ND license (http://creativecommons.org/licenses/by-nc-nd/4.0/).

1. Introduction

Waste glass (WG) is a promising supplementary cementitious material (SCM) because of its high silica content (approximately 70%). It was first used to supplant coarse aggregates in concrete in the 1960s, but it failed owing to the diminished mechanical property and the serious alkali-silica reaction (ASR) expansion [1,2]. Much research has been done to address this issue such as lowering the particle size of WG [3–5]. The pozzolanic property of glass particles increased and was even better than fly ash when it was ground into less than 100 μm [6,7]. Corinaldesi, et al. [8] reported that waste glass powder (WGP) with particle size ranging from 36 to 100 μm, both improved mechanical strength and reduced ASR expansion. Besides, the combination of WGP with pozzolans (fly ash, silica fume, metakaolin, etc.) can alleviate the deleterious expansion [9–11].

The previous studies mainly focused on the particle size and use of supplementary materials with WGP [8,12,13]. Although chemical activation is effective, the investigation is rarely reported due to the complexity of category and amount of chemical activator [14–16]. Besides, it is time-consuming and inaccurate for the traditional design method by summarising rules and phenomena to find the optimal mix composition when coping with multiple variables [17–19]. Therefore, the artificial intelligence (AI) based multi-objective optimisation model is proposed to determine optimal values of variables including the particle size and replacement proportion of WGP, and the category and amount of chemical activator.

To this end, machine learning (ML) models are introduced, such as artificial neural network (ANN) and support vector regression (SVR) [20–22]. They are widely used in data mining, having excellent generalisation ability, rapid computations, and high prediction accuracy [23,24]. However, both ANN and SVR are standalone ML models and possess a higher probability of overfitting the dataset and worse tolerance to outliers and noise than ensemble ML models such as the random forest (RF) model [25,26]. Therefore, the RF model is chosen for data prediction. However, it has a downside about its hyperparameters which are hard to adjust using conventional methods. Thus, optimisation algorithms have been introduced to automatically find the optimal hyperparameters, such as genetic algorithm (GA), particle swarm optimisation (PSO), and firefly algorithm (FA) [27–31]. Because the FA algorithm can eliminate the effect of multimodality and automatic subdivision, it is selected to optimise the hyperparameters of the RF model [32–34].

The FA-RF-based multi-objective optimisation (MOFA-RF) is established to optimise the mixture proportions utilizing a metaheuristic algorithm because of its simple codes and high efficiency in solving complicated engineering problems [35,36]. Compared to the single-objective optimisation method, MOFA-RF can optimise multiple objectives (UCS, ASR, cost, etc.) simultaneously under highly nonlinear constraints by proposing Pareto solutions [37,38]. Huang, et al. [39] used FA based bi-objective model to estimate the optimal mixture of steel fiber reinforced concrete. Zhang, et al. [25] optimised three objectives (strength, slump, and cost) using a multi-objective PSO algorithm. The multi-objective optimisation design is also promising to combine with updated technology such as Building Information Modeling [40,41] and 3D-printing technology [42].

Concrete containing waste glass can also be utilized for other applications such as radiation shielding, which is worth being further investigation [43]. The ZnO concentration has a significant effect on the mechanical and shielding properties of tellurite glasses [44]. Meanwhile, its radiation attenuation characteristics can be improved by the addition of TeO_2 and Sb_2O_3 [45,46]. Al-Buriahi et al. [47] demonstrated that Ag_2O and WO_3 had little effect on the mechanical properties of the $TeO_2 - Ag_2O - WO_3$ glass system, but their content had a significant influence on the shielding properties. In addition, lead sodium borate glass modified with chromium oxide offers good shielding properties against gamma, electron, and neutron radiation [48]. The addition of silver oxide causes a decrease in the molar polarizability and an increase in the light transmission of $Ag_2O–MoO_3–V_2O_5–TeO_2$ (AMVT) glass [49]. Olarinoye simulated the effect of $Ag_2O/\ V_2O_5$ substitution on the radiation shielding ability of tellurite glass systems using XCOM and FLUKA [50]. The $TeO_2 - Na_2O - TiO$ glass system was also investigated with the PHITS Monte Carlo procedure and proved to be an excellent nuclear shielding material [51].

In this study, the main focus is the effect of mechanical, chemical, and mechanical-chemical activation of WGP on the UCS and ASR characteristics of mortar. As the variables of the physical activation, the WGP with an average size of 75 μm and 300 μm was selected to supplant sand by 10%, 20%, and 30%. The chemical activators were salt activator (sodium sulfate), and alkaline activator (calcium hydroxide and sodium hydroxide). The Scanning Electron Microscopy (SEM) was employed for the study of ASR expansion and microstructure analysis. Then, the MOFA-RF was set up to optimise bi-objective mixture proportions based on the datasets of UCS (or ASR) and the objective function of cost. A sensitive study was finally carried out to find the degree of dependency of results on variables. This investigation is aimed at providing a feasible glass activation method and optimal mixture design of WGP mortar.

2. Experimental program

2.1. Materials

WGP was 75 μm and 300 μm in size on average coming from transparent waste bottles. The bottles were supposed to be pretreated so that the labels and contaminations were eliminated, followed by air-drying and grinding the bottles using a ball mill. The prepared WGP was then stored in a sealed container. Figure 1a and b shows the appearance of WGP in two different sizes. The strength grade of Ordinary Portland cement was 42.5 with the specific gravity, fineness index, and normal consistency around 3 t/m^3, 390 m^2/kg, and 27% respectively. The natural sand with over 96% silicon dioxide was graded as per ASTM C778 [52].

The chemical composition of WGP and cement obtained by X-ray Fluorescence Spectrometer (XRF) are listed in Table 1. Statistically, WGP has a large pozzolanic potential due to the high content of silica dioxide (74.02%).

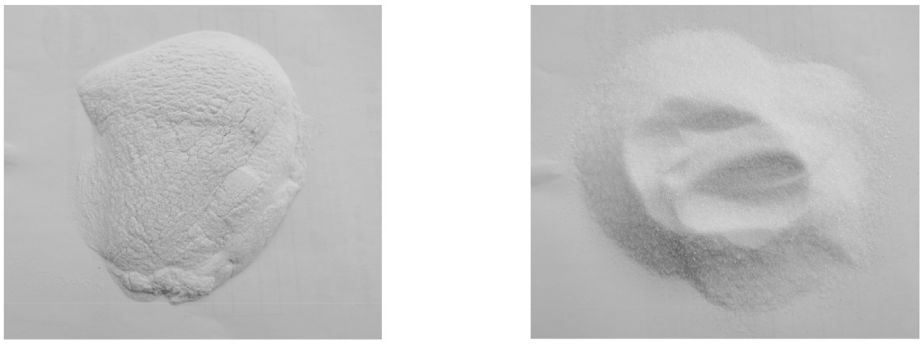

Fig. 1 – The distinctive features of WGP with the mean particle size of (a) 75 μm and (b) 300 μm.

2.2. *Composite mixture design*

In this study, the variables included the size and proportion of WGP and the amounts of chemical activators. WGP was used to replace natural sand with 10wt%, 20wt%, and 30wt%. The water to cement ratio and filler (sand + WGP) to cement ratio were fixed to 0.47 and 2.25, respectively. The following activation methods were used:

a. Mechanical activation: The waste glass with a mean particle size of 300 μm was ground to 75 μm using a ball mill. The finer WGP was predicted to possess better pozzolanic properties.
b. Chemical activation: The chemical activators were sodium sulfate (anhydrous), sodium hydroxide, and calcium hydroxide. The commercially available analytically pure (AR) grade was used. A 1:1 w/w mixture of sodium hydroxide and calcium hydroxide was used as an alkaline activator, and sodium sulfate was used as a salt activator. The proportion of both was 2%, 4%, and 6% by mass of cement. Sodium sulfate and sodium hydroxide were dissolved in mixing water in proportion. However, calcium hydroxide, a slightly soluble material, was mixed with the WGP, and then blended with cement and sand. The mixing procedure for mortar production complied with ASTM C305.
c. Mechanical-chemical (combined) activation: For this approach, the mechanical and chemical activation methods were combined. The WGP was ground transforming from 300 μm to 75 μm, and chemical activators were added as described in method b.

Table 1 – Chemical compositions of WGP and cement.

WGP		General Purpose Cement	
Chemical composition		**Chemical composition**	
SiO_2	74.02%	SiO_2	20.10%
Al_2O_3	1.40%	Al_2O_3	4.60%
Fe_2O_3	0.19%	Fe_2O_3	2.80%
CaO	11.25%	CaO	63.40%
MgO	3.34%	MgO	1.30%
SO_3	0.33%	SO_3	2.70%
Na_2O	9.03%	Na_2O	0.60%
K_2O	0.29%	Total chloride	0.02%

In Table 2, the detailed mixing proportions were listed for each mix. In this table, letters G, S, H stands WGP, sodium sulfate, and alkali, respectively. The numbers 75 and 300 mean the average particle size of WGP is 75 μm and 300 μm. The number 10, 20, 30 after the letter G means 10%, 20%, and 30% sand replacement by WGP. And the number 2, 4, 6 after letters S and H demonstrates the content of sodium sulfate and alkali with 2%, 4%, and 6%, respectively.

2.3. *Unconfined compressive test*

The UCS test was conducted for three parallel specimens for each mix at 7, 14, and 28 curing ages. Cubic specimens with 50 × 50 × 50 mm in size were used for the test as per ASTM C109. After casting, the sample was immediately stored in a moist room for 24 hours with plastic sheets covered. Subsequently, the specimen was removed from the molds and then immersed in a saturated lime water tank for 7, 14, and 28 days. The unconfined compression test was conducted on samples shortly after being taken out of the storage tank. The experimental setup is presented in Fig. 2 with the loading rate set as 0.6 MPa/s.

2.3.1. *Alkali silica reaction*

According to ASTM C1260, the potential risk of ASR expansion was evaluated by monitoring the longitudinal change of mortar bar samples. For each mix, three specimens were prepared and the average longitudinal change ratio would be recorded. The prismatic sample was cast in size of 25 × 25 × 280 mm. Two steel stud gauges were equipped at both ends, reducing the initial effective length to 260 mm. The figure of mortar bar samples is shown in Fig. 3. The 80 °C temperature and 1N sodium hydroxide solution was used to accelerate ASR as per ASTM C1260.

The bar specimens were prepared with the required aggregate grading specified by ASTM C1260. After casting, the molds were immediately transferred to the moisture room curing for 24 hours. Then, they were removed from the molds and directly placed in 80 °C water for another 24 hours. After immersing, the length of the bar sample was determined as the initial length L_0 by using a length comparator and a digital indicator accurate to 0.002 mm, shown in Fig. 4. Afterward, the bar specimens were transferred to 1N NaOH solution at 80 °C.

Table 2 – Mixing proportions for waste glass mortar.

Specimen ID	Cement (g)	Natural sand (g)	Water (g)	WGP (g)	Na_2SO_4 (g)	Alkali (g)
C (control sample)	450	1012.5	211.5	0	0	0
Waste glass powder (75 μm)						
75G10	450	911.25	211.5	101.25	0	0
75G10S2H2	450	911.25	211.5	101.25	9	9
75G10S2H4	450	911.25	211.5	101.25	9	18
75G10S2H6	450	911.25	211.5	101.25	9	27
75G10S4H2	450	911.25+	211.5	101.25	18	9
75G10S4H4	450	911.25	211.5	101.25	18	18
75G10S4H6	450	911.25	211.5	101.25	18	27
75G10S6H2	450	911.25	211.5	101.25	27	9
75G10S6H4	450	911.25	211.5	101.25	27	18
75G10S6H6	450	911.25	211.5	101.25	27	27
75G20	450	810	211.5	202.50	0	0
75G20S2H2	450	810	211.5	202.50	9	9
75G20S2H4	450	810	211.5	202.50	9	18
75G20S2H6	450	810	211.5	202.50	9	27
75G20S4H2	450	810	211.5	202.50	18	9
75G20S4H4	450	810	211.5	202.50	18	18
75G20S4H6	450	810	211.5	202.50	18	27
75G20S6H2	450	810	211.5	202.50	27	9
75G20S6H4	450	810	211.5	202.50	27	18
75G20S6H6	450	810	211.5	202.50	27	27
75G30	450	708.75	211.5	303.75	0	0
75G30S2H2	450	708.75	211.5	303.75	9	9
75G30S2H4	450	708.75	211.5	303.75	9	18
75G30S2H6	450	708.75	211.5	303.75	9	27
75G30S4H2	450	708.75	211.5	303.75	18	9
75G30S4H4	450	708.75	211.5	303.75	18	18
75G30S4H6	450	708.75	211.5	303.75	18	27
75G30S6H2	450	708.75	211.5	303.75	27	9
75G30S6H4	450	708.75	211.5	303.75	27	18
75G30S6H6	450	708.75	211.5	303.75	27	27
Waste glass powder (300 μm)						
300G10	450	911.25	211.5	101.25	0	0
300G10S2H2	450	911.25	211.5	101.25	9	9
300G10S2H4	450	911.25	211.5	101.25	9	18
300G10S2H6	450	911.25	211.5	101.25	9	27
300G10S4H2	450	911.25	211.5	101.25	18	9
300G10S4H4	450	911.25	211.5	101.25	18	18
300G10S4H6	450	911.25	211.5	101.25	18	27
300G10S6H2	450	911.25	211.5	101.25	27	9
300G10S6H4	450	911.25	211.5	101.25	27	18
300G10S6H6	450	911.25	211.5	101.25	27	27
300G20	450	810	211.5	202.50	0	0
300G20S2H2	450	810	211.5	202.50	9	9
300G20S2H4	450	810	211.5	202.50	9	18
300G20S2H6	450	810	211.5	202.50	9	27
300G20S4H2	450	810	211.5	202.50	18	9
300G20S4H4	450	810	211.5	202.50	18	18
300G20S4H6	450	810	211.5	202.50	18	27
300G20S6H2	450	810	211.5	202.50	27	9
300G20S6H4	450	810	211.5	202.50	27	18
300G20S6H6	450	810	211.5	202.50	27	27
300G30	450	708.75	211.5	303.75	0	0
300G30S2H2	450	708.75	211.5	303.75	9	9
300G30S2H4	450	708.75	211.5	303.75	9	18
300G30S2H6	450	708.75	211.5	303.75	9	27
300G30S4H2	450	708.75	211.5	303.75	18	9
300G30S4H4	450	708.75	211.5	303.75	18	18
300G30S4H6	450	708.75	211.5	303.75	18	27
300G30S6H2	450	708.75	211.5	303.75	27	9
300G30S6H4	450	708.75	211.5	303.75	27	18
300G30S6H6	450	708.75	211.5	303.75	27	27

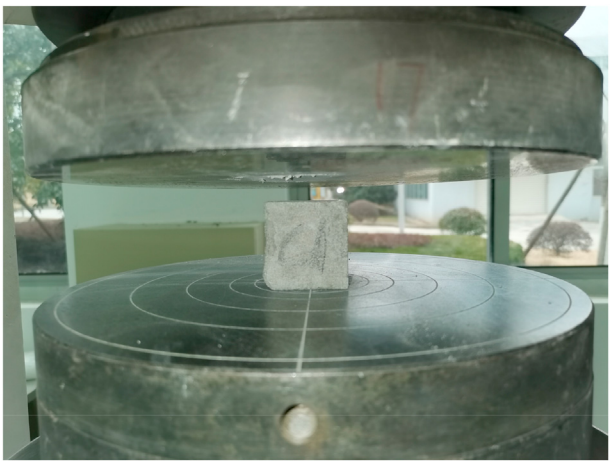

Fig. 2 – The experimental setup for the UCS test.

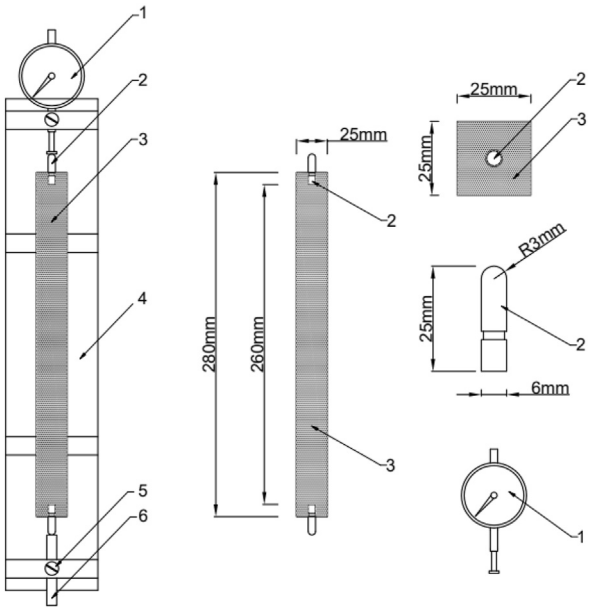

1-Steel stud gauge; 2-Metal gauge studs; 3-Mortar-bar; 4-Aluminum alloy base; 5-Fastening screw; 6-Locating rod

Fig. 4 – Schematic figure of ASR expansion test.

The length of the bar sample was measured at 2, 4, 7, 10, and 14 days within 15±5s after it was removed from the alkali lye. The bar length at day x is denoted by L_x and the ASR expansion ratio e can be calculated by Equation (1).

$$e = \frac{L_x - L_0}{260} \times 100\% \quad (1)$$

2.3.2. *Scanning electron microscopy*

SEM was utilized for exploring the microstructure of the WGP and WGP-cement system. The WGP samples (75 μm) were pretreated before testing as shown in Table 3. The mortar specimens were directly taken from the fragments of samples (75G10 and 75G10S2H2) after the compression test.

3. Multi-objective optimisation methodology

The optimal mixture design of activated WGP mortar adopts the methodology of MOFA-RF. The process is depicted in Fig. 5. Overall, this multi-objective design started from the construction of two RF models for the prediction of UCS and ASR with the hyperparameters tuned by FA and 10-fold cross-validation (CV). Then, the cost was calculated for each mix. The weighted sum method was used for establishing a multi-

Table 3 – Details of the preparation of SEM samples of WGP.

WGP Specimen	Pretreatment			
	WGP (g)	Na_2SO_4 (g)	50% NaOH +50% $Ca(OH)_2$ (g)	Water (g)
G	50	–	–	100
G (2%alkali+2% Na_2SO_4)	50	4.3	4.3	100

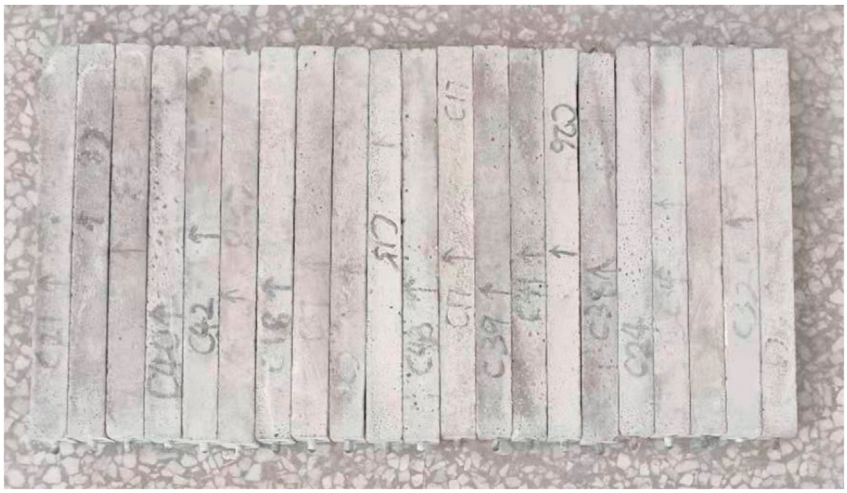

Fig. 3 – Bar samples for ASR expansion test.

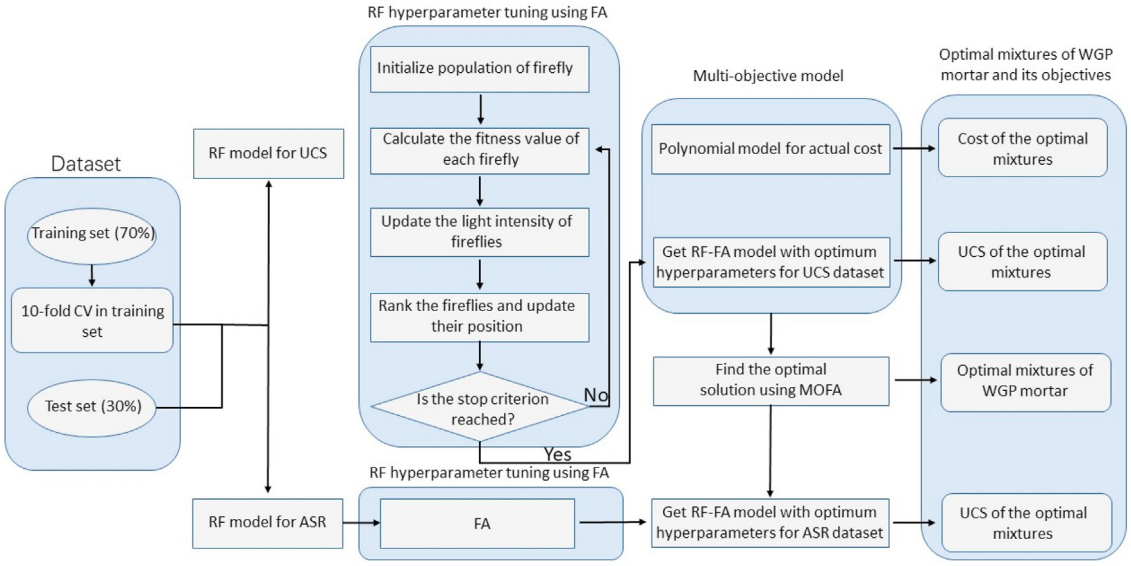

Fig. 5 – Flowchart of the MOFA-RF system for WGP-mortar optimisation design.

Table 4 – Statistics of input and output variables for the UCS dataset.

Variables	Minimum	Maximum	Mean	Std Dev
WGP size (μm)	75	300	187.5	112.79
WGP (kg/m^3)	0	382.73	249.61	107.09
Sodium sulfate (kg/m^3)	0	33.42	22.11	11.04
Alkali (kg/m^3)	0	33.36	22.11	11.03
Sand (kg/m^3)	868.5	1262.91	999.36	104.62
Age (day)	7	28	22.5	8.75
UCS (MPa)	6.82	35.72	18.64	5.93

objective function and the Pareto front was produced to show the optimisation mixture design of WGP mortar.

3.1. *Data description*

As mentioned above, the variables are the size and proportion of WGP and the content of chemical activators. The dataset is sourced from the results from UCS and ASR expansion tests and they are served as the output variables. The statistics of input and output variables are listed in Table 4 for UCS and Table 5 for ASR.

Table 5 – Statistics of input and output variables for the ASR dataset.

Variables	Minimum	Maximum	Mean	Std Dev
WGP size (μm)	75	300	187.5	112.64
WGP (kg/m^3)	0	382.73	249.61	106.94
Sodium sulfate (kg/m^3)	0	33.42	22.11	11.03
Alkali (kg/m^3)	0	33.36	22.11	11.01
Sand (kg/m^3)	868.5	1262.91	999.36	104.47
Age (day)	0	14	5.5	4.78
ASR (%)	0	0.1592	0.0462	0.04

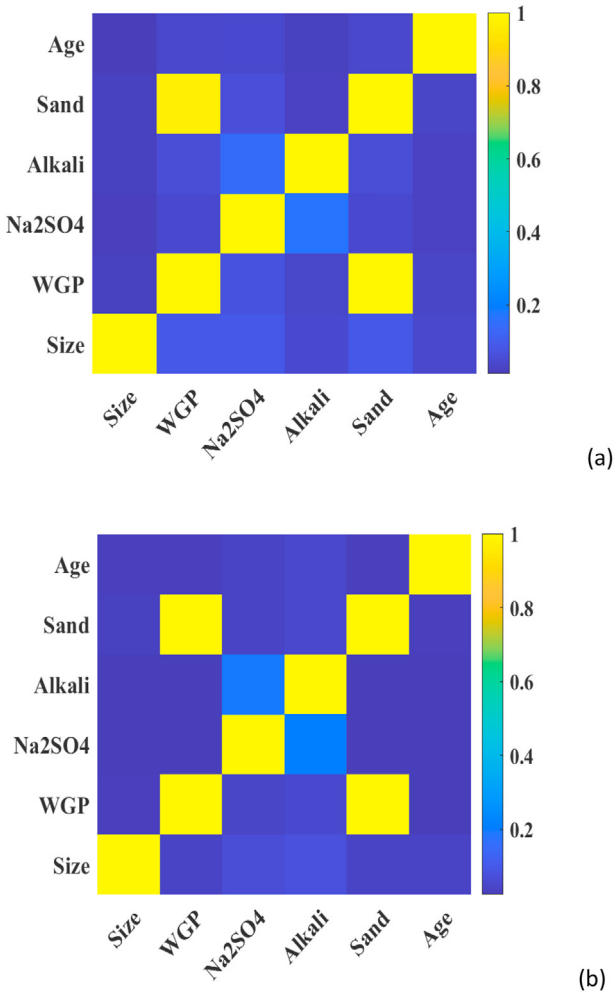

Fig. 6 – Correlation matrix of input variables for (a) UCS dataset (b) ASR dataset.

The figures of correlation between different input variables of UCS and ASR datasets are shown in Fig. 6. The correlation between sand and WGP was high because the WGP was in replacement of sand by 10% to 30%. Therefore, the ratio of WGP to sand and cement was used to conduct the variable importance analysis. While for multi-objective optimisation (MOO) analysis, the amount of each raw material had to be represented instead of the ratio. The other correlation values were low enough that the input variables were independent so that the multicollinearity problems could be effectively eliminated in this study.

3.2. *Establishment of FA-RF model*

3.2.1. *Random forest model*

RF model combines multiple results from different regression trees (RTs) using the bagging method and can obtain the final results via voting. The training procedure of the RF model is described as shown in Fig. 7 where R_n^{θ} stands for a bootstrap sample including n samples. These samples are from the training set and each of them is selected randomly with $^1/_n$ probability. Besides, θ and k are independently distributed vectors and the number of RTs respectively. These regression trees are trained to predict the respective values: $\hat{a}$ (x, $R_n^{\theta_1}$), $\hat{a}$ (x, $R_n^{\theta_2}$), …, $\hat{a}$ (x, $R_n^{\theta_k}$) on corresponding k bootstrap samples {$R_n^{\theta_1}$, $R_n^{\theta_2}$, …, $R_n^{\theta_b}$}. The prediction outcome will be finally acquired from the average results of the k RTs.

3.2.2. *Firefly algorithm*

The firefly algorithm is derived from the social behaviour of fireflies. Fireflies are attracted to the brightness, so the brighter firefly, the more attractive it is to others. However, the attractiveness of brightness decreases as the distance between two fireflies increases. The brightest firefly flies randomly through the surrounding area. Eventually, it will be observed because the other fireflies continuously travel towards it. The brightness depends on the objective function of a specific problem. Equation (2) shows the position change of firefly i moving towards firefly j which has a higher brightness.

$$x_i^{t+1} = x_i^t + \beta_0 e^{-\gamma r_{ij}^2}\left(x_j^t - x_i^t\right) + \alpha(rand - 1/2) \quad (2)$$

$$r_{ij} = x_j^t - x_i^t \quad (3)$$

In the above function, $\mathbf{x}_i^t$ and $\mathbf{x}_j^t$ are the positions of two fireflies i and j at the t-th iteration. Besides, r_{ij} in Equation (3) shows the Euclidian distance between the positions of the two fireflies and β_0 means the highest attractiveness of the firefly when r equals zero. Since the brightness reduces with distance and medium, γ is introduced as an absorption coefficient to represent this situation, ranging from 0 to 1. The other parameters α and *rand* are the randomization parameter and random vector derived from the Gaussian distribution, ranging from 0 to 1. The pseudocode of FA can be shown in Fig. 8.

3.3. *Hyperparameter tuning*

3.3.1. *Cross fold validation*

In the RF model, two hyperparameters need to be optimised. The first one is *numTree* which means the total number of regression trees trained for the dataset. It significantly influences the computation efficiency and the generalisation ability. Another hyperparameter is *minNumLeaf* showing the minimum sample number of a leaf node and shows the correlation between regression trees.

One of the challenges in the modeling process is to eliminate the overfitting problems. Thus, a 10-fold CV was proposed to comprehensively assess the data in this study. The data were randomly divided into two groups comprising

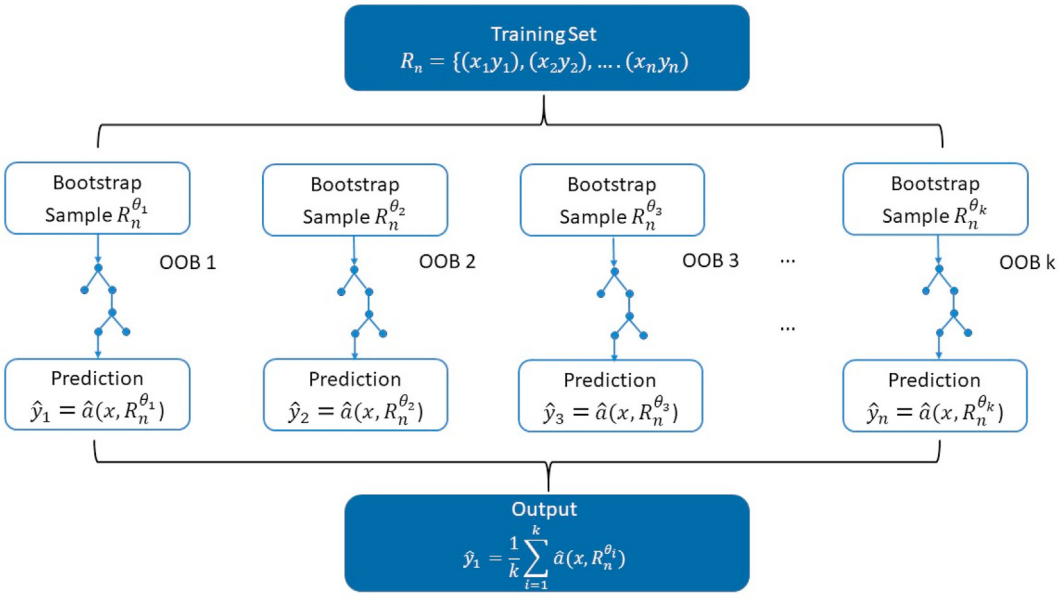

Fig. 7 – Construction of an RF model.

testing sets (30%) and training sets (70%). The training data was split into 10 folds, nine of which were used for machine learning, and the remaining one was used for the validation of the model performance as shown in Fig. 9. During this process, the root means square error (RSME) could be obtained. The optimal hyperparameters were subsequently determined after the completion of 50 iterations. The above process was repeated 10 times with a non-repetitive validation fold chosen at each time. Ultimately, the RF model with the minimum RSME and corresponding optimal hyperparameters were applied to predict the results of testing sets.

3.3.2. *Performance assessment*

Evaluation is essential in measuring the accuracy of the model. In this research, RMSE, correlation coefficient (R), mean absolute error (MAE), and mean absolute percentage error (MAPE) were the evaluation indices. They are defined in the following equations.

$$RSME = \sqrt{\frac{1}{n}\sum_{i=1}^{n}\left(y_i^* - y_i\right)^2} \tag{4}$$

$$\mathrm{MAE} = \frac{1}{n}\sum_{i=1}^{n}\left|y_i^* - y_i\right| \tag{5}$$

$$\mathrm{MAPE} = \frac{1}{n}\sum_{i=1}^{n}\left|\frac{y_i^* - y_i}{y_i}\right| \tag{6}$$

$$\mathrm{R} = \frac{\sum_{i=1}^{n}\left(y_i^* - \overline{y^*}\right)\left(y_i - \overline{y}\right)}{\sqrt{\sum_{i=1}^{n}\left(y_i^* - \overline{y^*}\right)^2}\sqrt{\sum_{i=1}^{n}\left(y_i^* - \overline{y}\right)^2}} \tag{7}$$

where n means the n groups of data samples; y_i^* and y_i demonstrate the predicted and actual values; $\overline{y^*}$ and $\overline{y}$ are the mean values of the predicted and actual data, respectively.

3.4. *Multi-objective optimisation*

3.4.1. *Objective function establishment*

The cost was also included for the MOO design. A polynomial function shown in Equation (8) was used to calculate the cost of mortar containing WGP.

$$Cost\left(\$/m^3\right) = C_c Q_c + C_w Q_w + C_d Q_d + C_G Q_G + C_S Q_S + C_H Q_H \tag{8}$$

In the above equation, C is the unit price ($/kg) of the materials used in mortar production and Q represents the quantity (kg/m^3) of different raw materials. The cost of cement, water, silica sand, WGP, and chemical activators is listed in Table 6 in which all the prices are the average local retailing price.

3.4.2. *Constraints of variables*

To solve multi-objective optimisation problems, several constraints are set including mortar volume constraint, range constraint of materials, and ratio constraint, shown in Equation (9) and Table 7. The price of WGP mortar is calculated based on one cubic meter to unify the unit. The input variables are summarized for their minimum and maximum values and three ratio constraints are also determined for calculating Pareto optimal solutions.

$$V_m\left(1m^3\right) = \frac{Q_c}{U_c} + \frac{Q_w}{U_w} + \frac{Q_d}{U_d} + \frac{Q_G}{U_G} + \frac{Q_S}{U_S} + \frac{Q_H}{U_H} \tag{9}$$

where U is the unit weight of materials.

3.4.3. *Construction of MOFA-RF*

The establishment of MOFA-RF is based on the objective functions of UCS, ASR, and cost by applying the weighted sum method. The UCS and ASR are combined with cost separately to set up a function as shown in Equation (10).

Begin
Define objective function $f(x)$, $x = (x_1, \ldots, x_d)^T$
Set the search space, total number of generation, and fireflies
Obtain light intensity I_i at x_i by $f(x_i)$
Set light absorption coefficient
Generate initial population, $k = 0$
While $(t \leq maxGeneration)$ **do**
    Update the generation number, $k = k + 1$
    Tune randomisation parameter using adaptive inertia weight
    Tune attractiveness parameter using Guass/mouse chaotic map
        for $i = 1$: no. fireflies
            for $j = 1$: no. fireflies
                if $(I_j > I_i)$
                    move firefly i toward j by levy flight
                end if
                change attractiveness with distance r
            end for j
        end for i
        Rank the fireflies and find the current best
end while
Obtain results
End

Fig. 8 – The pseudocode of FA.

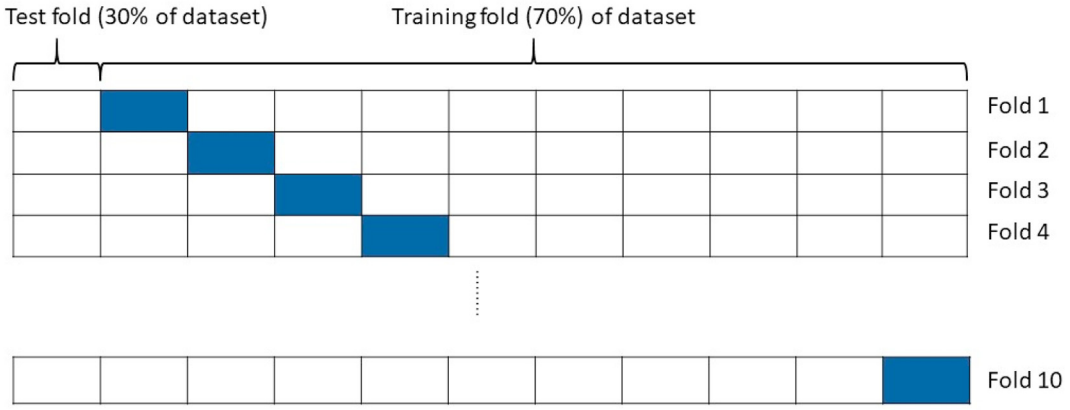

Fig. 9 – 10-fold cross-validation.

Table 6 – Price of different materials.

Materials	Notation	Unit Price ($/kg)	Unit weight (kg/m^3)
Cement	C_c	0.057	3000
Water	C_w	0.001	1000
Silica sand	C_d	0.038	2300
Waste glass powder	C_G	0.087	2450
Sodium sulfate	C_S	0.143	2680
Alkali	C_H	0.69	2185

Table 7 – Constraints of input variables.

Variables	Expressions	Lower bound	Upper bound
WGP size	S	75	300
Sodium sulfate	C_S	0	27
Alkali	C_H	0	27
WGP ratio	$C_G/(C_G+C_d)$	0	0.3
WGP to cement ratio	C_G/C_c	0	0.675
Sand ratio	C_d/C_c	1.575	2.25

$$f = \sum_{i=1}^{i} w_i f_i \,,\ \sum_{i=1}^{i} w_i = 1 \tag{10}$$

where f_i means the multiple objectives; f is the combined function in solving MOO problem; w_i equals to p_i/i where the denominator is the random number arising from a uniform distribution [0,1] and the numerator is the uniformly distributed number.

The above equation can be formulated in the following manner in this research.

$$f_1 = w_1 \cdot UCS + w_2 \cdot cost \tag{11}$$

$$f_2 = w_1 \cdot ASR(14\ days) + w_2 \cdot cost \tag{12}$$

$$\sum_{i=1}^{2} w_i = 1 \tag{13}$$

To solve the optimisation problem, Pareto optimal front is determined since the dual objectives are supposed to be minimized or maximized simultaneously [53]. They represent

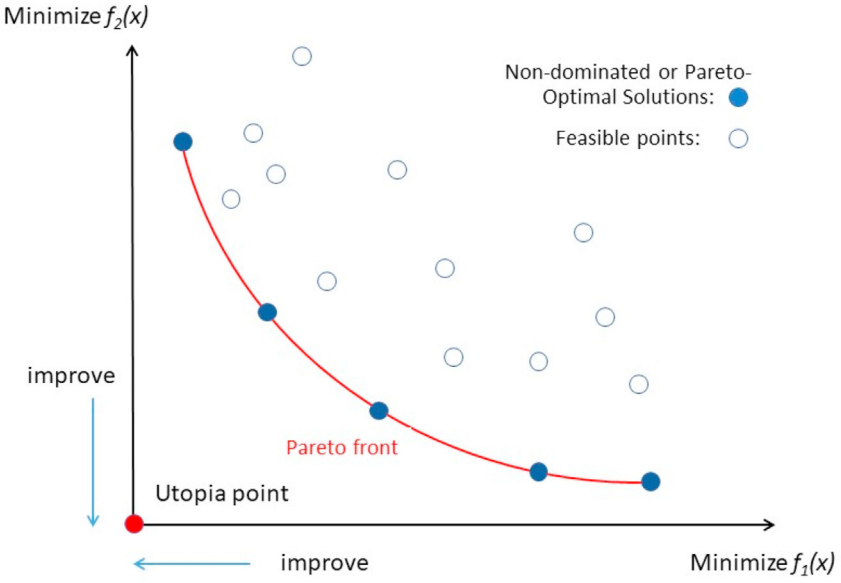

Fig. 10 – The schematic diagram of Pareto optimal solutions.

Begin
Define objective function $f_1(x),\ f_2(x), \ldots, f_k(x); x = (x_1, \ldots, x_d)^T$
Generate initial population of fireflies $x_i = (i = 1,2, \ldots, n)$
Determine light intensity I_i at x_i by $f(x_1)$
Set light absorption coefficient

While
  for $i, j = 1{:}n$ (all n fireflies)
    Evaluate the approximations of PF_i and PF_j to the Pareto front
      if PF_j dominates PF_i,
        Move firefly from i to j
        Generate new ones if constraints are not satisfied
      end if
      if no non-dominated solutions can be found
        Generate random weights $w_k(k = 1, \ldots K)$
        Find the best solution that can minimise the combined objective
        Random walk around the best solution
      end if
      Update and pass the non-dominated solutions to the next iterations
  end
  Sort and find the current best approximation to the Pareto front
  Update t
end while
Post process results and visualisation

Fig. 11 – The pseudocode of MOFA-RF.

the solutions that are non-dominated so that any of the other objective functions fail to be improved without harming another function [54]. The mathematical expression for Pareto optimum is formed as follows [55].

If $\mathbf{x}^* \in S$ is Pareto optimal solution, whereby S is the set of feasible solutions, the nonexistence of $x \in S$ such that

$$f_i(x) \leq f_i(x^*) \text{ for } i = 1, 2, 3, \ldots, k \text{ and} \quad (14)$$

$$f_i(x) < f_i(x^*) \text{ for at least one value } i \quad (15)$$

The set of the non-dominated Pareto optimal solutions constitutes the Pareto front that the connection of blue points depicts a line if the number of objective functions is two, shown in Fig. 10. Apart from the Pareto front, the other feasible points would not be optimal since their objective function values are larger than at least one point in the Pareto front. The FA can be developed to MOFA-RF to calculate Pareto optimal solutions for finding optimisation mixture design. The pseudocode of MOFA-RF is summarised in Fig. 11.

3.5. *Variable importance measure*

In some cases where the concrete expression is unavailable, this blocks the visualisation of the relationship between the input variables and the outcome. Thus, this study uses a method based on sensitivity analysis (SA) to assess and rank the influence of the inputs on the outputs. Sensitivity analysis is a method commonly used to qualitatively or quantitatively evaluate the dependence of results on variables by measuring the change in outputs caused by input disturbances [56,57]. It includes both local and global analysis, which allows the effect of either a single variable or multiple variables on outputs. Global sensitivity analysis (GSA) is preferred in this study because it allows multiple variables to be altered simultaneously so that a ranking of importance among variables can be obtained. Equations (16) and (17) are the calculations where the variable 'a' changes in the range of the input dataset while the other variables remain constant at their mean values.

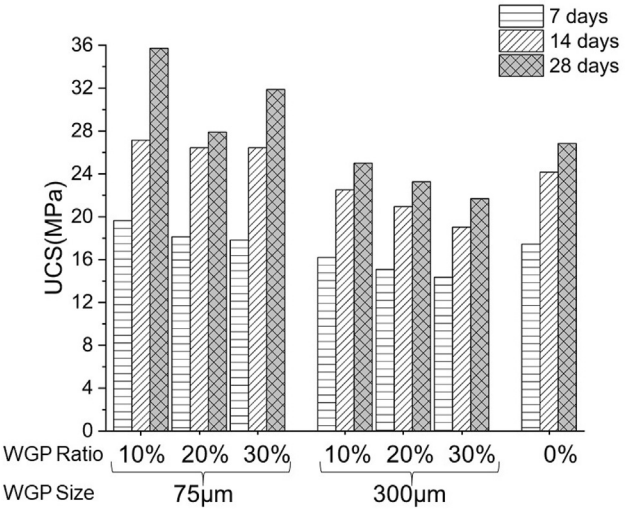

Fig. 12 – The UCS of mortar containing WGP with different proportions by mechanical activation at different curing ages.

$$G_a = \sum_{j=2}^{L} \frac{\left|\widehat{y_{a,j}} - \widehat{y_{a,j-1}}\right|}{N-1} \quad (16)$$

$$R_a = G_a \Big/ \sum_{i=1}^{I} G_i \quad (17)$$

where G_a is the average difference between adjacent outputs $\widehat{y_{a,j}}$ and $\widehat{y_{a,j-1}}$; N is the number of the value of the variable under research; R_a is the relative importance of the variable 'a'.

4. Results and discussion

4.1. Results of laboratory tests

4.1.1. Result of unconfined compression test

The outcome of the compression test for mortar samples with different WGP (75 μm and 300 μm) replacement ratios is depicted in Fig. 12. The UCS decreased with the increase of 300 μm WGP content, which is inconsistent with previous

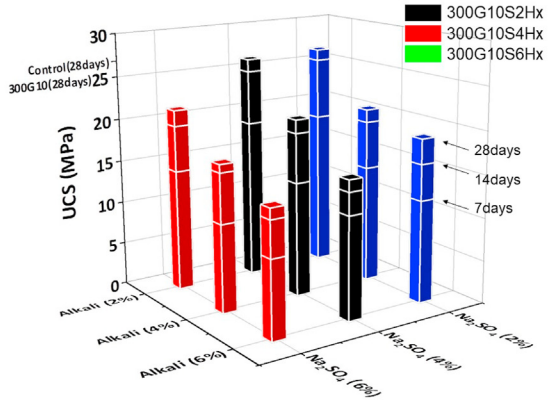

(a)

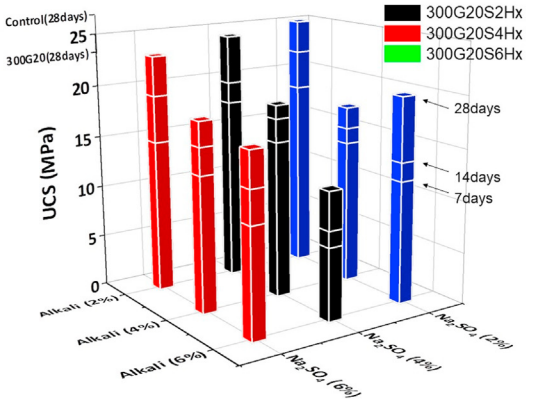

(b)

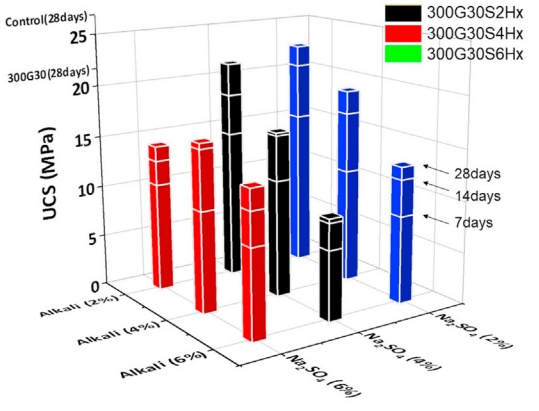

(c)

Fig. 13 – The UCS of mortar containing WGP (300 μm) at (a) 10% (b) 20% (c) 30% by chemical activation.

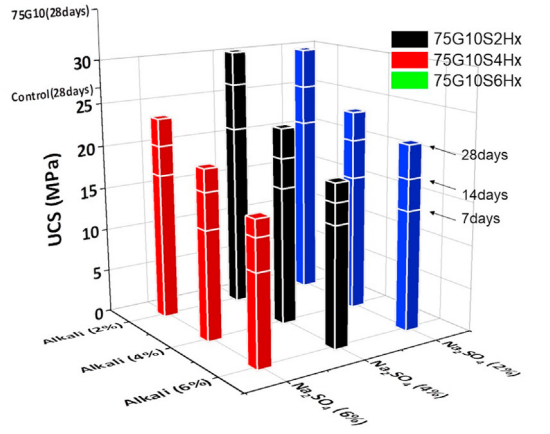

(a)

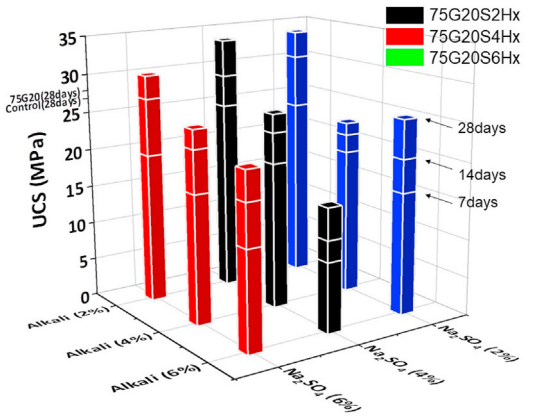

(b)

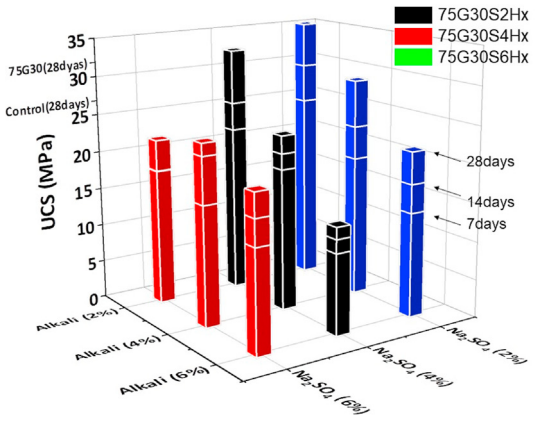

(c)

Fig. 14 – The UCS of mortar containing WGP (75 μm) at (a) 10% (b) 20% (c) 30% by mechanical-chemical activation.

results demonstrating the negative influence of using coarse glass powder as the filler. The strength of mortars containing fine glass powder (75G10, 75G20, 75G30) was greater than that of the samples with coarse WGP (300G10, 300G20, 300G30) for all curing times and replacement ratios. This demonstrated the positive influence of mechanical activation on UCS by reducing the particle size of the WGP. Besides, the 28-day UCS for mortars with 75 μm WGP showed higher strength than the control sample, mainly due to the relationship between the increase in cementitious performance and the decrease in strength caused by the loss of aggregates [6,27]. In fine WGP, the silica tetrahedron structure is less stable than in coarse WGP [58]. Therefore, the pozzolanic reaction for finer WGP is supposed to be more intense. Meanwhile, the finer WGP can be evenly dispersed into the pores of the mortar samples to increase their density and compactness. Therefore, mechanical activation is a promising approach to increase strength without changing its chemical composition [58,59].

Figure 13 shows the UCS of specimens containing 300 μm WGP for 10%, 20%, and 30% in replacement of sand under chemical activation. The combination of 2% alkali and 2% Na_2SO_4 was optimal on activating coarse WGP mortar. Compared to non-activated samples (300G10, 300G20, and 300G30), the 28-day UCS for samples prepared by this method was higher by approximately 6.6%, 7.9%, and 4.2%, respectively. The strength improvement can be attributed to the combined action of salt and alkali. Na_2SO_4 tends to react with $Ca(OH)_2$ to generate gypsum and NaOH. The gypsum then reacts with aluminate to form ettringite (AFt) and $Ca(OH)_2$. NaOH and WGP can generate an additional gel phase [60]. This leads to increased hydration which compacts the mortar samples and improves their strength. The efficacy of alkali is mainly because of the depolymerisation of the WGP structure by the alkali, contributing to the dissolution of active silica [61,62]. If the cations within the alkaline solution are Na^+ and Ca^{2+}, the N–C–S–H gel tends to form on the surface of the WGP [63]. However, excessive alkali content in the cement system can form heterogeneous gels and increase harmful expansion [64]. Also, excessive Na_2SO_4 would result in decreased compression strength, as too much AFt with a loose structure would be produced. Furthermore, the negative effect caused by an excess of alkali was greater than excessive Na_2SO_4, especially when the proportion of WGP was 20%, shown in Fig. 13b.

Figure 14 shows the UCS of specimens containing 75 μm WGP with 10%, 20% and 30% replacement ratios under activation of alkali and Na_2SO_4. Similarly, 2% Na_2SO_4 combined with 2% alkali was the best choice for both 20% and 30% WGP specimens. However, for mortar containing 10% fine glass powder, strength was only increased at the 7-day stage and decreased after that. In Fig. 14a, the 28-day UCS of 75G10S2H2 was 29.84 MPa and it was about 16.5% lower than 75G10 (35.72 MPa). This might be because gels propagated around the surface of the WGP, causing non-uniform voids to form over time [65]. Out of all the mixes, the highest 28-day UCS was found in the sample made from 30% 75 μm WGP chemically activated by 2% Na_2SO_4 and 2% alkali, standing at 35.33 MPa (31.6% higher than the control sample). Therefore, the mechanical-chemical activation is optimal, especially for the 30% WGP replacement ratio.

4.1.2. *Result of alkali-silica activation test*

The change of ASR expansion of mortars with different proportions of WGP (75 μm and 300 μm) is depicted with ages in Fig. 15. Generally, the expansion increased with an increase of WGP for both particle sizes. However, coarse WGP samples had higher expansion than fine WGP samples. The ASR expansion of samples containing WGP with all proportions

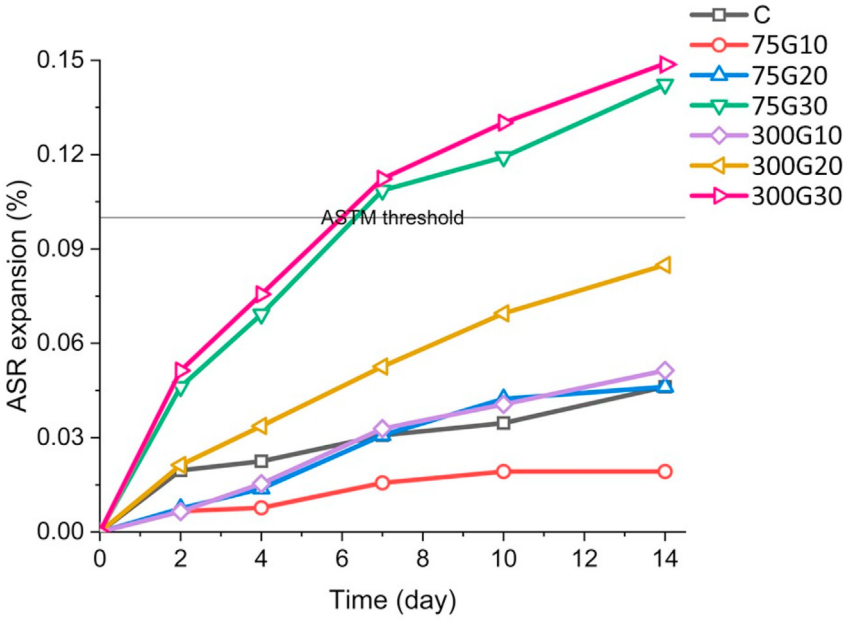

Fig. 15 – The ASR of mortar containing WGP (10%, 20%, 30%) with mechanical activation.

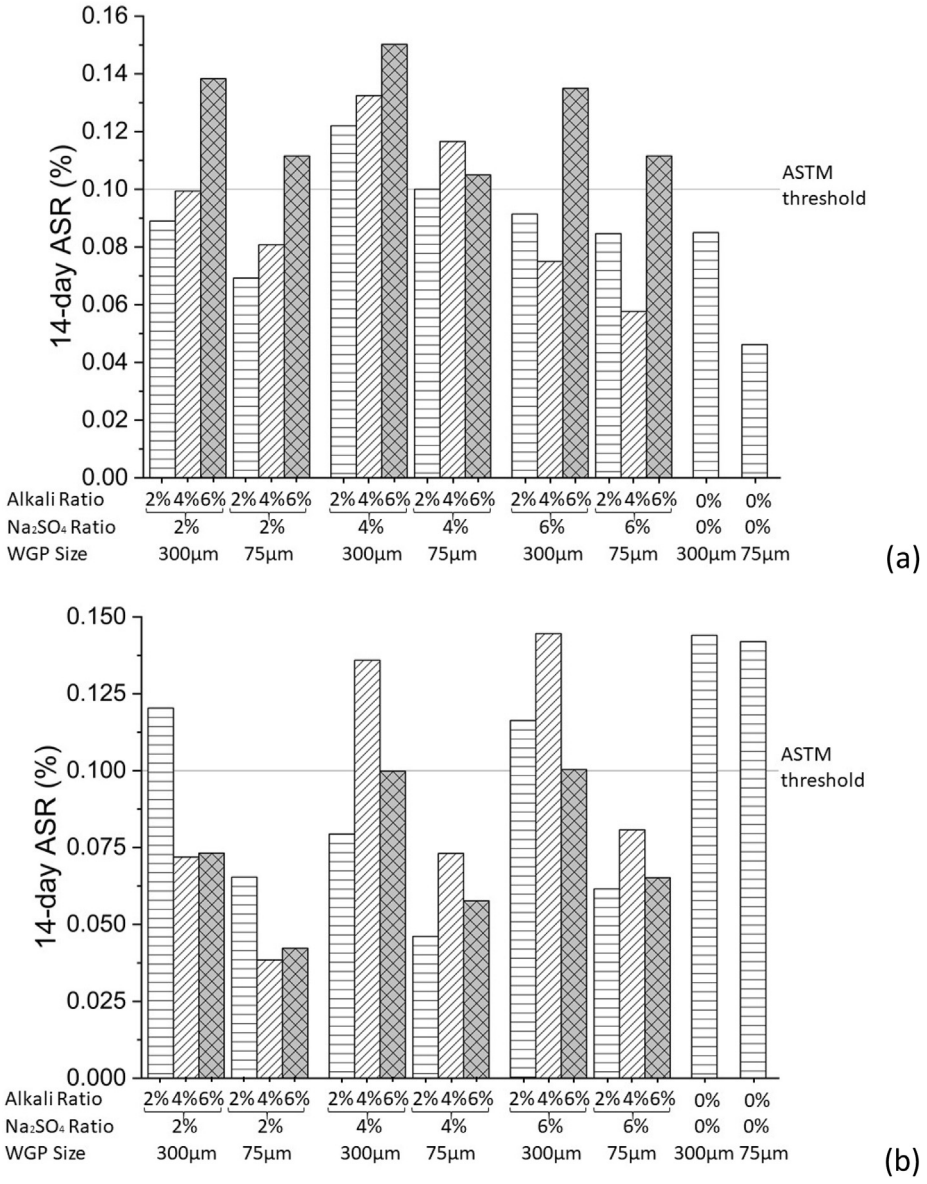

Fig. 16 – The 14-day ASR values of bar samples containing WGP (75, 300 μm) in the proportion of (a) 20% (b) 30% after being chemical activated.

was higher than that of the control sample, illustrating the adverse influence of the coarse glass powder. This observation is in good agreement with previous findings. For bar samples with 10% 75 μm WGP, the expansion was effectively mitigated. One of the plausible reasons is that the pozzolanic reaction of finer WGP tends to generate non-swelling gels [66]. However, the 14-day expansion was 0.1423% for the 30% 75 μm WGP specimen, exceeding the ASTM threshold (0.1%). This seems to contradict the published findings that finer WGP did not cause expansion [67,68]. This might be due to the micro-cracking in glass powder giving rise to high ASR expansion [69]. Although the exact cause is not clear, the mechanical activation has nonetheless proved to effectively mitigate the deleterious ASR expansion.

Figure 16 depicts the values of ASR expansion (14 days) for coarse and fine WGP with 20% and 30% substitute ratios to analyse the efficacy of chemical activation. The results of 10% WGP mortar samples are not depicted because they are generally larger than the ASTM threshold.

Generally, the trend for ASR for mortars containing 75 and 300 μm WGP particle sizes was similar. In samples with 20% chemical activated WGP, the efficacy of the chemical activator was negative as shown in Fig. 16a. Conversely, when the WGP content was increased to 30%, the ASR values of both 300 μm and 75 μm chemical activated WGP bars were lower than 300G30 (0.144%) and 75G30 (0.142%), respectively in Fig. 16b. The 14-day ASR value of the sample with 30% 75 μm WGP activated by 2% Na_2SO_4 and 2% alkali showed 55% lower than

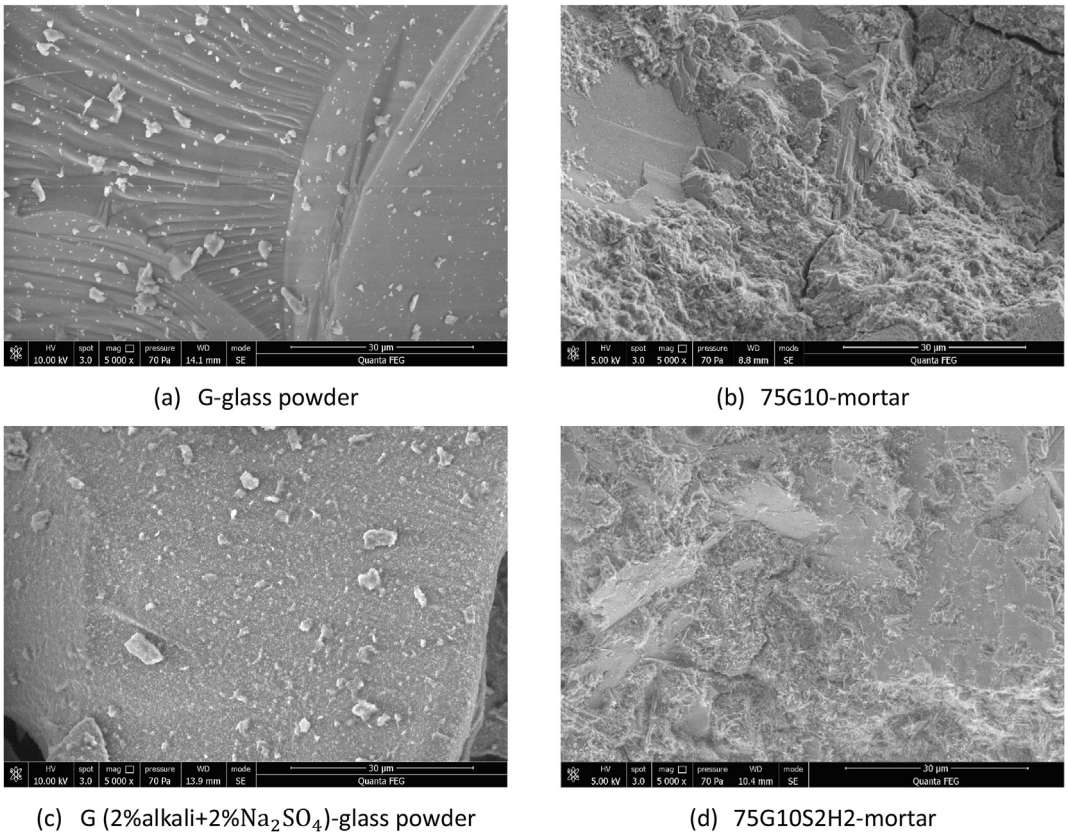

Fig. 17 – SEM micrographs of WGP (75 μm) and mortar.

30% 300 μm WGP sample. The reason might be that the higher concentration of calcium ions generated gels with lower swelling capacity since the alkaline activator contained calcium hydroxide [14,63]. However, the trend varying with the amount of alkali and Na_2SO_4 was hard to describe. Thus, a machine learning model was needed to simulate the tendency, as demonstrated in the next section. In conclusion, to control the 14-day ASR expansion within allowed the range (lower than 0.1%) as per ASTM C1260, 30% 75 μm WGP is preferred if the chemical activation approach is needed.

4.1.3. *Result of SEM*

Figure 17 shows the SEM results of WGP (75 μm) and mortar samples with and without being activated by 2% alkali+2% Na_2SO_4. SEM analysis presented the smooth surface of non-activated WGP with few tiny crystals attached. An obvious erosion reaction was observed on the surface when it was exposed to Na_2SO_4 and the alkaline solution as shown in Fig. 17c. Plenty of flocculent deposits were generated on the surface accompanied by calcium hydroxide crystals, indicating the susceptibility of the WGP to alkali.

The microstructural images of the mortars show the hydration product and their cementation on the WGP. The mortar sample with 2% alkali and 2% Na_2SO_4 exhibited a finer and denser structure with fewer fissures and voids than the non-activated WGP sample, shown in Fig. 17d. Besides, fewer CH crystals were found on 75 μm chemical activated WGP mortar samples than non-activated ones, indicating greater pozzolanic capacity. This confirms that the combination of mechanical grinding with 2% alkali and 2% Na_2SO_4 had higher strength than the control sample. In conclusion, the combined activation enhances the pozzolanic reaction of WGP and simultaneously compacts the mortar structure, while the amount of chemical activator is essential.

4.2. *Results of multi-objective optimisation design*

4.2.1. *Results of hyperparameter tuning*

As mentioned above, the two hyperparameters of the RF model (*numTree*, *minNumLeaf*) were tuned using FA and CV. The optimal fold within 10 folds CV provided the minimum RMSE as shown in Fig. 18. The minimum RMSE was observed at the 9th fold on the UCS dataset and the 6th fold on the ASR dataset. The optimal RMSE was obtained by iterations several times. In UCS and ASR datasets, 12 and 25 iterations were required to the convergency of RMSE respectively, illustrating the feasibility and efficiency of tuning the hyperparameters by FA (see Fig. 19). Finally, the optimal hyperparameters (*numTree*, *minNumLeaf*) were 26 and 1 for the UCS dataset, and 27 and 1 for the ASR dataset, respectively.

4.2.2. *Performance of FA-RF*

Figure 20a and Fig. 20b intuitively depict the prediction situation by FA-RF models for UCS and ASR respectively. The closer the points are to the black solid diagonal line, the smaller the difference between actual and predicted values.

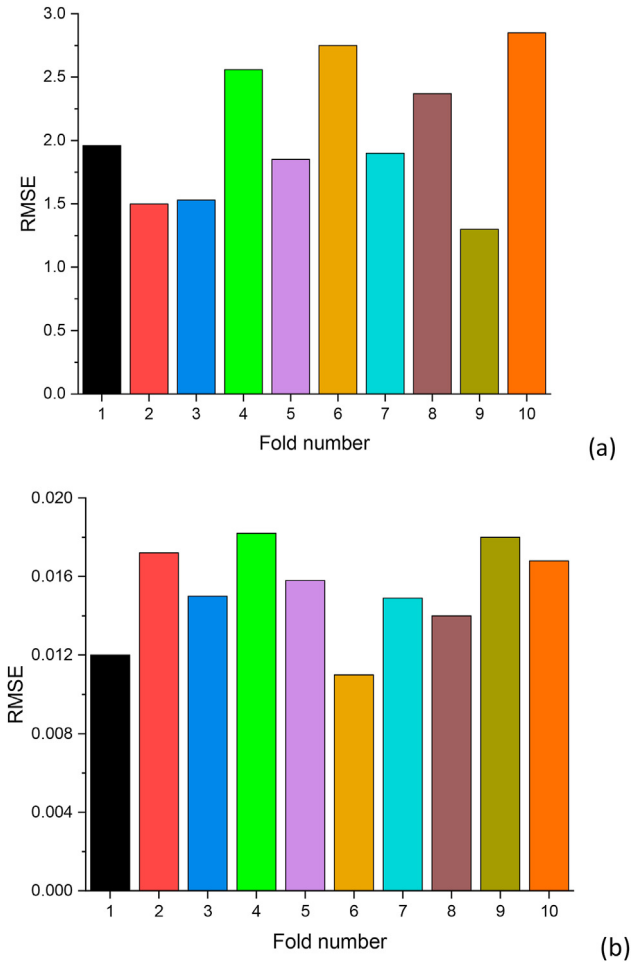

Fig. 18 – 10-fold CV for hyperparameters tuning on the (a) UCS dataset and (b) ASR dataset.

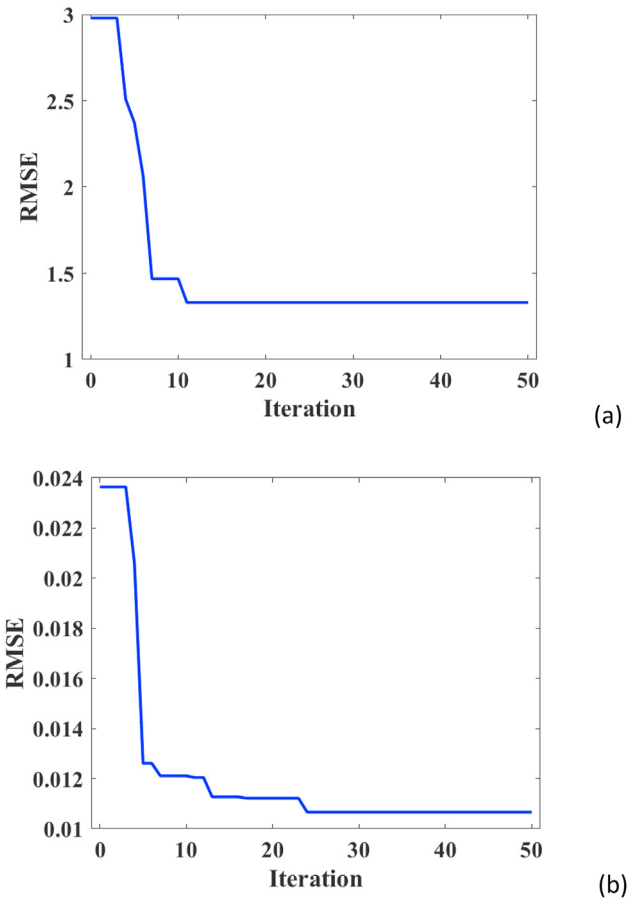

Fig. 19 – RMSE versus iteration in the optimal fold for (a) UCS dataset and (b) ASR dataset.

Most points are around the line apart from several outliers, indicating good prediction ability of the FA-RF model for both UCS and ASR datasets.

Table 8 summarizes the values of four evaluation indices (R, RMSE, MAE, and MAPE) of the FA-RF models on the test set for the prediction of UCS and ASR. The MAPE of the ASR dataset was unattainable since the actual value of ASR expansion was zero at zero curing time. The R values were found as 0.93 and 0.91, showing the robust correlation between the predicted and actual results. Besides, RMSE, MAE, and MAPE were all low for both models. And the values of RMSE or R on the training set and test set were both close which means that the overfitting issue did not happen. These numbers showed the credibility of FA-RF giving accurate predictions for UCS and ASR.

4.2.3. *WGP-mortar mixture optimisation design*

The Pareto front obtained by MOFA-RF was shown in Fig. 21 giving the non-dominated optimal solutions for UCS and cost or ASR (14 days) and cost based on the dataset and constraints. In Fig. 21a, multiple points with the same cost or UCS were observed since it was possible to increase the strength without increasing the cost or decrease the cost without decreasing the strength. The seven points (No. 9, 12, 13, 14, 15, 17, 18) with the better UCS or cost are identified. Before point 9, the UCS of WGP mortar was improved without increasing the cost, indicating that the strength of the mortar was capable to be significantly increased by changing the mixture with the unchanged total price. However, the higher UCS can only be achieved by increasing the cost. For point 18 with the highest UCS (30.54 MPa) in Fig. 21a, the price was predicted to be around 99.08 $\$/m^3$. While for point 9, 28.45 MPa compression strength could be reached with a lower price (78.84 $\$/m^3$). The selection is dependent on the decision-maker to measure the priority between the strength grade and budget.

Similarly, the Pareto optimal solutions for ASR and cost in Fig. 21b provides four points 5, 6, 9, and 17. The higher cost corresponds to the lower ASR value. However, the ASR value failed to be reduced to lower than 0.0287% although the cost continuously increased. Gaps were also observed in both Pareto fronts which were due partly to the limitation of the

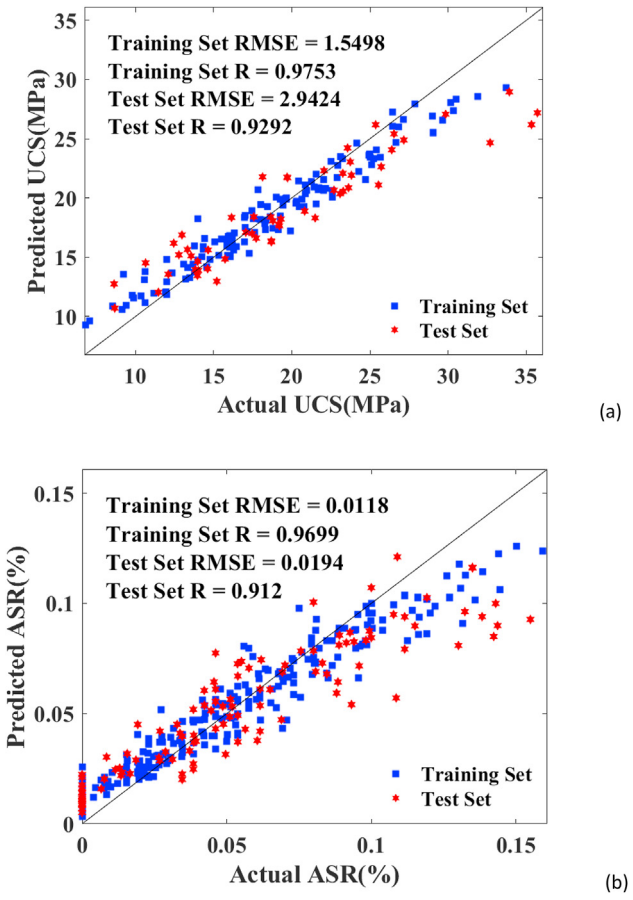

Fig. 20 – Actual versus predicted values for (a) UCS and (b) ASR.

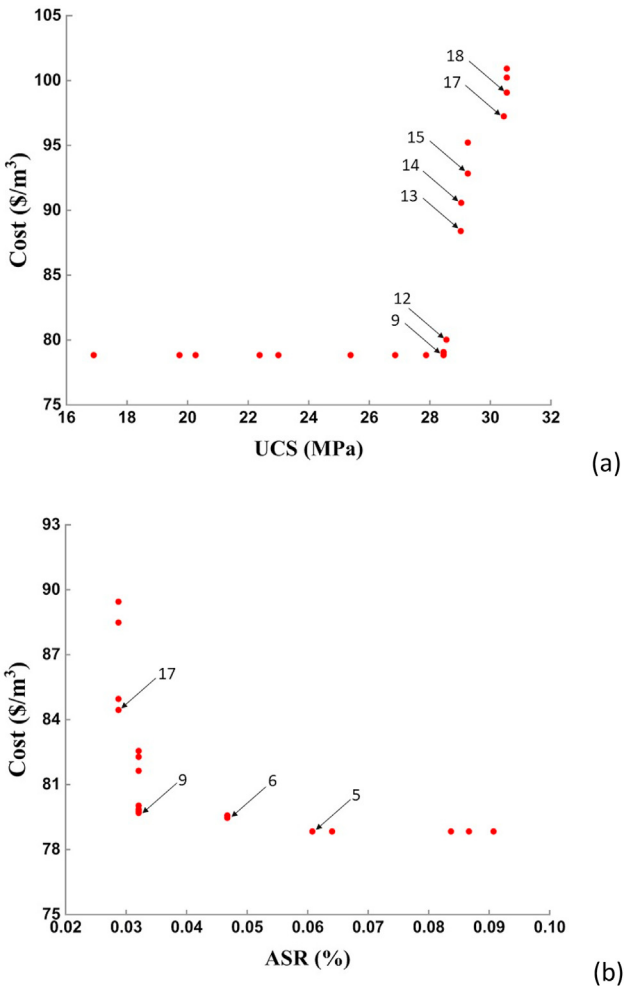

Fig. 21 – Pareto front based on Cost and (a) UCS or (b) ASR.

current dataset and partly to the finite number of Pareto points. This can be resolved by obtaining more data from different mixture designs or by generating more Pareto points with a longer computation time. The estimation of a suitable curve to link all the Pareto optimal solutions could also be used to approximate the results.

Table 9 and Table 10 list the UCS, ASR, cost, and efficiency ratio of the Pareto points. The efficiency ratio was calculated as the rise of the cost divided by the increase of the UCS or the decrease of the ASR. The lower efficiency ratio indicates the lower cost for improved UCS or reduced ASR expansion. For UCS, the efficiency ratio of point 9 was zero, showing that the cost of 78.84 $/m^3 maximised the UCS up to 28.45 MPa in these Pareto solutions. However, the efficiency ratio for point 14 was 108.5 which was the highest among the Pareto points so that the cost efficiency was low. For ASR, compared to the efficiency

Table 8 – Evaluation of FA-RF on UCS and ASR test sets.

Test category	Evaluation index			
	RMSE (MPa)	R	MAE (MPa)	MAPE
UCS	2.942	0.929	2.214	0.115
ASR	0.019	0.912	0.015	–

Table 9 – Pareto optimal solutions for UCS.

Number of points	UCS (MPa)	Cost ($/m^3)	Efficiency ratio
1	16.90	78.84	–
2	19.73	78.84	–
3	20.27	78.84	–
4	22.38	78.84	–
5	23.00	78.84	–
6	25.38	78.84	–
7	26.86	78.84	–
8	27.88	78.84	–
9	28.45	78.84	0
10	28.45	79.00	–
11	28.45	79.07	–
12	28.55	80.03	11.90
13	29.02	88.40	17.81
14	29.04	90.57	108.5
15	29.26	92.83	10.27
16	29.26	95.21	–
17	30.44	97.24	3.74
18	30.54	99.08	18.40
19	30.54	100.23	–
20	30.54	100.91	–

Table 10 – Pareto optimal solutions for ASR.

Number of points	ASR (%)	Cost ($)	Efficiency ratio
1	0.0907	78.84	–
2	0.0867	78.84	–
3	0.0837	78.84	–
4	0.0640	78.84	–
5	0.0608	78.84	0
6	0.0467	79.46	43.97
7	0.0467	79.55	–
8	0.0467	79.58	–
9	0.0321	79.69	15.75
10	0.0321	79.73	–
11	0.0321	79.80	–
12	0.0321	79.86	–
13	0.0321	80.03	–
14	0.0321	81.64	–
15	0.0321	82.28	–
16	0.0321	82.56	–
17	0.0287	84.45	1400
18	0.0287	84.95	–
19	0.0287	88.48	–
20	0.0287	89.45	–

ratio of 1400 for point 17, the other three points (No. 5,6,9) stood at 0, 43.97, and 15.75 respectively. The ratios were relatively low, indicating the high-cost efficiency. Notably, a gradual increase was observed between these three points in Fig. 21b.

Generally, the Pareto front provides multi-objective optimisation choices, and it is up to the decision-maker to decide on the budget and the appropriate strength and expansion. Point 9 and in point 5 in UCS-cost and ASR-cost Pareto solutions are also good choices, since the efficiency ratios of both are zero, representing the most cost-effective situation.

4.2.4. *Variable importance of using FA*

The importance scores of variables based on the UCS and ASR dataset arising from the sensitivity study were transferred to the importance ratios as shown in Fig. 22. The content of alkali

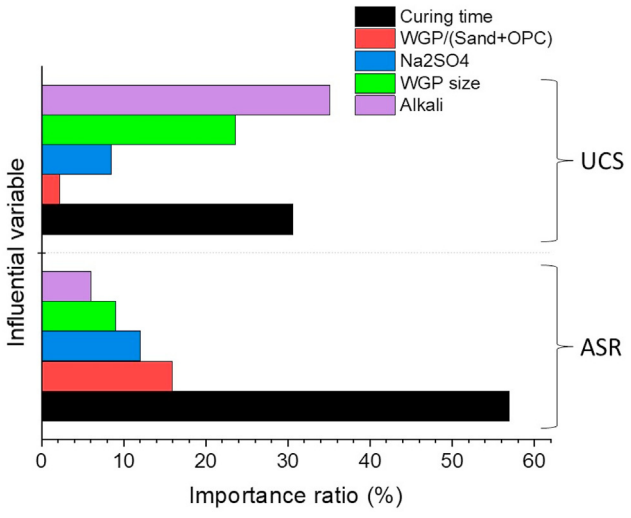

Fig. 22 – Input variables importance measure for UCS and ASR of WGP-mortar mixture design.

was found to be the input variable with the greatest influence on UCS, accounting for 35%. It verified the author's previous finding that the content of alkali had a higher influence than the amount of Na_2SO_4. Curing time was the second most influential variable, which is reasonable since later UCS was larger than early UCS. This was followed by the particle size of the glass powder, indicating that finer UCS possessed better pozzolanic properties, leading to greater strength. However, Na_2SO_4 content and the replacement ratio of WGP seem less important than other variables, standing at 8.58% and 1.67%, separately. This further confirms the importance of the particle size of the WGP and shows that the reduced strength caused by a higher amount of WGP could be offset by introducing a chemical activator, provided the amount was suitable.

For the ranking of input variables for ASR expansion, the variable with the highest importance ratio is curing time, since the expansion was observed to increase rapidly with a longer testing time. This was followed by the WGP replacement ratio, as the expansion of 30% WGP (75 μm, 300 μm) bar samples was found to be much larger than that of samples containing 10% and 20% WGP. In contrast with the study on the importance of UCS, alkali content was found to be the least influential factor for ASR expansion, because the mortar bar test was conducted in an environment with a high concentration of alkali. The amount of Na_2SO_4 and the particle size of glass powder was also less important than curing time and WGP ratio. In conclusion, the importance measure provides a valuable analysis to compare all the input variables. Apart from curing time, the content of alkali and WGP replacement ratio are the most important parameters for UCS and ASR respectively.

5. Conclusions

In this study, UCS and ASR expansion tests were conducted on mortar samples where part of sand was replaced by WGP treated by mechanical, chemical, and mechanical-chemical, activation. The SEM images were used to investigate the microstructure of WGP and mortar samples. Besides, a FA-RF based multi-objective optimisation model was set up to estimate the optimal mixture design for UCS, cost, and ASR cost. The following results were drawn from this study:

1. The UCS of the WGP mortar specimen was significantly improved by the mechanical method. The chemical activation was less effective and adversely affected the UCS when the amounts of chemical additives were excessive. The mechanical-chemical activation was optimal that the highest UCS was observed at 35.33 MPa (31.6% higher than the control sample) in the mortar specimen containing 30% 75 μm WGP activated by 2% Na_2SO_4 and 2% alkali.
2. Mechanical activation effectively mitigated ASR expansion. Chemical activation was better when the WGP replacement ratio was 30%. The ASR of 75 μm WGP mortar sample activated by 2% Na_2SO_4 and 2% alkali was 55% lower than 30% 300 μm WGP sample, illustrating the effectiveness of the mechanical-chemical activation.

3. SEM results showed that when WGP was exposed to the chemical activator, its surface underwent a significant erosion reaction and produced a large number of flocculated deposits with calcium hydroxide crystals. Additionally, the combined activated WGP mortar samples exhibited a finer and denser structure with fewer fissures and voids than the non-activated ones.
4. The firefly algorithm was competent in tuning hyperparameters of the RF model with minimum RMSE obtained at the 9th and 6th fold on the UCS and ASR dataset respectively. The R values for the UCS and ASR test set were 0.93 and 0.91, indicating their high accuracy in predicting UCS and ASR.
5. The MOFA-RF successfully measured the Pareto fronts for dual objectives (UCS, cost, and ASR, cost) with nonlinear constraints. It provides a guide of multi-objective optimisation designs for the decision-maker. The design with the lowest efficiency ratio (point 9 for the UCS-cost set and point 5 for the ASR-cost set) means the highest cost-efficiency.
6. The generalisation ability of MOFA-RF can be improved by producing more Pareto solutions and collecting a comprehensive database. Furthermore, the set constraints can be adjusted to be more suitable for real engineering works.
7. The variable importance ranking determined by the RF shows that the most significant variables were alkali content and curing time, affecting respectively UCS and ASR, which is consistent with the experimental findings.

Declaration of Competing Interest

The authors declare that they have no known competing financial interests or personal relationships that could have appeared to influence the work reported in this paper.

Acknowledgments

This research was funded by the Academic Research Council of Australia Linkage Projects for Asset Intelligence: Maximising Operational Effectiveness for Digital Era, (Grant No. LP180100222). This study was also funded by the Jiangsu 2020 Students' innovation and entrepreneurship training program (202011276014Z, 202011276011Z) and 2021 Students' innovation and entrepreneurship training program (202111276019Z, 202111276020Z).

Appendix A

ID	Compression strength (MPa)			ASR expansion (%)					
	7d	14d	28d	0d	2d	4d	7d	10d	14d
C	17.44	24.15	26.84	0	0.0196	0.0225	0.0308	0.0346	0.0462
75G10	19.64	27.14	35.72	0	0.0066	0.0077	0.0156	0.0192	0.0192
75G10S2H2	20.89	25.37	29.84	0	0.0346	0.0385	0.0519	0.0692	0.1038
75G10S2H4	15.83	20.32	23.63	0	0.0154	0.0214	0.0315	0.0577	0.0731
75G10S2H6	13.97	17.63	21.50	0	0.0246	0.0308	0.0446	0.0538	0.0808
75G10S4H2	21.24	26.54	30.34	0	0.0231	0.0292	0.0538	0.0984	0.1430
75G10S4H4	16.02	19.45	22.89	0	0.0154	0.0254	0.0538	0.0808	0.1308
75G10S4H6	13.98	16.46	18.64	0	0.0100	0.0231	0.0615	0.0885	0.1160
75G10S6H2	16.97	20.42	23.57	0	0.0038	0.0115	0.0462	0.0846	0.1192
75G10S6H4	12.78	17.04	19.66	0	0.0085	0.0231	0.0615	0.1077	0.1385
75G10S6H6	10.62	14.35	16.33	0	0.0046	0.0247	0.0462	0.0810	0.1000
75G20	18.13	26.44	27.90	0	0.0075	0.0138	0.0308	0.0423	0.0462
75G20S2H2	23.74	30.53	33.92	0	0.0157	0.0346	0.0385	0.0538	0.0692
75G20S2H4	19.21	21.55	23.12	0	0.0200	0.0386	0.0465	0.0612	0.0808
75G20S2H6	16.08	20.46	25.55	0	0.0538	0.0577	0.0713	0.0831	0.1115
75G20S4H2	24.96	29.01	33.73	0	0.0346	0.0538	0.0615	0.0756	0.1000
75G20S4H4	19.25	23.29	25.72	0	0.0385	0.0615	0.0885	0.1038	0.1166
75G20S4H6	9.23	11.99	16.15	0	0.0421	0.0731	0.0885	0.1077	0.1055
75G20S6H2	19.70	27.17	30.19	0	0.0077	0.0192	0.0500	0.0650	0.0846
75G20S6H4	17.04	22.70	25.22	0	0.0154	0.0260	0.0423	0.0462	0.0577
75G20S6H6	13.09	18.69	22.60	0	0.0385	0.0846	0.0962	0.1000	0.1115
75G30	17.82	26.44	31.88	0	0.0462	0.0692	0.1086	0.1192	0.1423
75G30S2H2	24.73	29.65	35.33	0	0.0154	0.0200	0.0269	0.0500	0.0654
75G30S2H4	18.65	22.95	29.05	0	0.0077	0.0085	0.0154	0.0231	0.0385
75G30S2H6	13.78	17.54	21.75	0	0.0154	0.0192	0.0231	0.0269	0.0423
75G30S4H2	22.03	25.65	32.69	0	0.0192	0.0288	0.0346	0.0427	0.0462
75G30S4H4	18.80	20.89	23.24	0	0.0346	0.0538	0.0577	0.0615	0.0731
75G30S4H6	10.65	12.45	14.01	0	0.0216	0.0386	0.0462	0.0538	0.0577
75G30S6H2	17.96	18.02	22.06	0	0.0208	0.0269	0.0346	0.0513	0.0615
75G30S6H4	15.96	22.16	23.82	0	0.0154	0.0346	0.0486	0.0692	0.0808
75G30S6H6	13.56	17.06	20.24	0	0.0268	0.0346	0.0462	0.0538	0.0652

Appendix B

ID	Compression strength (MPa)			ASR expansion (%)					
	7d	14d	28d	0d	2d	4d	7d	10d	14d
300G10	16.20	22.51	25.01	0	0.007	0.015	0.033	0.041	0.051
300G10S2H2	18.29	25.40	26.66	0	0.027	0.046	0.057	0.095	0.126
300G10S2H4	13.77	19.31	20.79	0	0.016	0.025	0.037	0.066	0.083
300G10S2H6	12.02	16.22	19.13	0	0.025	0.034	0.062	0.058	0.091
300G10S4H2	18.69	24.95	26.40	0	0.027	0.034	0.066	0.133	0.166
300G10S4H4	13.46	19.26	20.83	0	0.018	0.028	0.072	0.109	0.144
300G10S4H6	12.02	14.65	16.03	0	0.011	0.026	0.076	0.096	0.140
300G10S6H2	14.26	19.60	21.45	0	0.004	0.015	0.052	0.094	0.131
300G10S6H4	10.35	16.19	17.14	0	0.009	0.030	0.071	0.134	0.158
300G10S6H6	9.13	13.35	14.62	0	0.005	0.035	0.063	0.093	0.108
300G20	15.08	20.94	23.27	0	0.021	0.034	0.062	0.070	0.085
300G20S2H2	18.36	22.05	25.12	0	0.029	0.038	0.055	0.079	0.089
300G20S2H4	14.02	15.52	17.57	0	0.021	0.050	0.056	0.080	0.092
300G20S2H6	11.90	13.71	19.93	0	0.059	0.065	0.082	0.108	0.128
300G20S4H2	17.72	19.73	24.28	0	0.044	0.060	0.067	0.092	0.114
300G20S4H4	15.21	17.47	18.78	0	0.049	0.077	0.104	0.134	0.126
300G20S4H6	7.07	8.64	12.34	0	0.052	0.085	0.122	0.137	0.155
300G20S6H2	14.78	19.29	23.09	0	0.008	0.021	0.055	0.081	0.097
300G20S6H4	13.22	15.89	18.30	0	0.017	0.028	0.049	0.061	0.072
300G20S6H6	10.60	13.83	17.29	0	0.042	0.113	0.125	0.129	0.137
300G30	14.36	19.03	21.69	0	0.041	0.076	0.086	0.130	0.144
300G30S2H2	15.33	20.65	22.61	0	0.039	0.053	0.086	0.113	0.120
300G30S2H4	11.19	16.98	19.17	0	0.013	0.015	0.029	0.038	0.069
300G30S2H6	8.54	12.10	13.33	0	0.028	0.037	0.043	0.045	0.077
300G30S4H2	14.54	18.47	21.58	0	0.032	0.053	0.064	0.071	0.086
300G30S4H4	11.47	15.88	16.15	0	0.062	0.095	0.104	0.103	0.140
300G30S4H6	6.82	9.39	9.80	0	0.037	0.073	0.085	0.089	0.106
300G30S6H2	10.60	12.97	14.41	0	0.039	0.048	0.060	0.086	0.107
300G30S6H4	9.89	15.73	16.29	0	0.026	0.062	0.084	0.122	0.145
300G30S6H6	8.68	11.94	13.97	0	0.050	0.060	0.080	0.093	0.099

REFERENCES

[1] Federico L, Chidiac S. Waste glass as a supplementary cementitious material in concrete–critical review of treatment methods. Cement Concr Compos 2009;31(8):606–10.

[2] Sun J, Huang Y, et al. Mechanical enhancement for EMW-absorbing cementitious material using 3D concrete printing. J Build Eng 2021:102763.

[3] Nassar R-U-D, Soroushian P. Field investigation of concrete incorporating milled waste glass. J Solid Waste Technol Manag 2011;37(4):307–19.

[4] Zhao R, Zhang L, et al. Unveiling substitution preference of chromium ions in sulphoaluminate cement clinker phases. Compos B Eng 2021:109092. https://doi.org/10.1016/j.compositesb.2021.109092.

[5] Sun J, Aslani F, et al. Electromagnetic absorption of copper fiber oriented composite using 3D printing. Construct Build Mater 2021;300:124026. https://doi.org/10.1016/j.conbuildmat.2021.124026.

[6] Aly M, Hashmi M, et al. Effect of colloidal nano-silica on the mechanical and physical behaviour of waste-glass cement mortar. Mater Des 2012;33:127–35.

[7] Xu D, Liu Q, et al. Analytical approach for crack identification of glass fiber reinforced polymer–sea sand concrete composite structures based on strain dissipations. Struct Health Monit 2020. https://doi.org/10.1177/1475921720974290. 1475921720974290.

[8] Corinaldesi V, Gnappi G, et al. Reuse of ground waste glass as aggregate for mortars. Waste Manag 2005;25(2):197–201.

[9] Li J, Qin Q, et al. Mechanical and conductive performance of electrically conductive cementitious composite using graphite, steel slag, and GGBS. Struct Concr 2020. https://doi.org/10.1002/suco.202000617.

[10] Xu X, Wang C, Zhou P. GVRP considered oil-gas recovery in refined oil distribution: from an environmental perspective. Int J Prod Econ 2021;235:108078. https://doi.org/10.1016/j.ijpe.2021.108078.

[11] Feng J, Chen B, et al. Microbial induced calcium carbonate precipitation study using Bacillus subtilis with application to self-healing concrete preparation and characterization. Construct Build Mater 2021;280:122460. https://doi.org/10.1016/j.conbuildmat.2021.122460.

[12] Ali A, Zhang C, et al. Investigation of five different low-cost locally available isolation layer materials used in sliding base isolation systems. Soil Dynam Earthq Eng 2022;154:107127. https://doi.org/10.1016/j.soildyn.2021.107127.

[13] Zhang W, Tang Z. Numerical modeling of response of CFRP–concrete interfaces subjected to fatigue loading. J Compos Construct 2021;25(5):04021043. https://doi.org/10.1061/(ASCE)CC.1943-5614.0001154.

[14] Mou B, Bai Y. Experimental investigation on shear behavior of steel beam-to-CFST column connections with irregular panel zone. Eng Struct 2018;168:487–504. https://doi.org/10.1016/j.engstruct.2018.04.029.

[15] Xu J, Wu Z, et al. Study on strength behavior of basalt fiber-reinforced loess by digital image technology (DIT) and scanning electron microscope (SEM). Arabian J Sci Eng 2021;46(11):11319–38. https://doi.org/10.1007/s13369-021-05787-1.
[16] Wang D, Ju Y, et al. Mechanical properties of high performance concrete reinforced with basalt fiber and polypropylene fiber. Construct Build Mater 2019;197:464–73. https://doi.org/10.1016/j.conbuildmat.2018.11.181.
[17] Sun J, Wang Y, et al. Mechanical, chemical and hydrothermal activation for waste glass reinforced cement. Construct Build Mater 2021;301:124361.
[18] Liu W, Guo Z, et al. Physico-mechanical and microstructure properties of cemented coal Gangue-Fly ash backfill: effects of curing temperature. Construct Build Mater 2021;299:124011. https://doi.org/10.1016/j.conbuildmat.2021.124011.
[19] Wang L, Yuan J, et al. Practical algorithm for stochastic optimal control problem about microbial fermentation in batch culture. Optim Lett 2019;13(3):527–41.
[20] Sun J, Ma Y, et al. Machine learning-aided design and prediction of cementitious composites containing graphite and slag powder. J Build Eng 2021:102544.
[21] Sun J, Wang Y, et al. Machine-learning-aided prediction of flexural strength and ASR expansion for waste glass cementitious composite. Appl Sci 2021;11(15):6686.
[22] Wu C, Wang X, et al. Differential received signal strength based RFID positioning for construction equipment tracking. Adv Eng Inf 2019;42:100960. https://doi.org/10.1016/j.aei.2019.100960.
[23] Tsai Y-H, Wang J, et al. A BIM-based approach for predicting corrosion under insulation. Autom ConStruct 2019;107:102923.
[24] Hou L, Wu S, et al. Literature review of digital twins applications in construction workforce safety. Appl Sci 2021;11(1):339.
[25] Zhang J, Huang Y, et al. Multi-objective optimization of concrete mixture proportions using machine learning and metaheuristic algorithms. Construct Build Mater 2020;253:119208. https://doi.org/10.1016/j.conbuildmat.2020.119208.
[26] Liu J, Wu C, et al. A novel differential search algorithm and applications for structure design. Appl Math Comput 2015;268:246–69.
[27] Xu D-s, Huang M, Zhou Y. One-dimensional compression behavior of calcareous sand and marine clay mixtures. Int J GeoMech 2020;20(9):04020137. https://doi.org/10.1061/(ASCE)GM.1943-5622.0001763.
[28] Wang J, Dai Q, Si R. Experimental and numerical investigation of fracture behaviors of steel fiber–reinforced rubber self-compacting concrete. J Mater Civ Eng 2022;34(1):04021379. https://doi.org/10.1061/(ASCE)MT.1943-5533.0004010.
[29] Chou J-S, Ngo N-T, Pham A-D. Shear strength prediction in reinforced concrete deep beams using nature-inspired metaheuristic support vector regression. J Comput Civ Eng 2016;30(1):04015002.
[30] Luo Y, Zheng H, et al. Fatigue reliability evaluation of aging prestressed concrete bridge accounting for stochastic traffic loading and resistance degradation. Adv Struct Eng 2021;24(13):3021–9. https://doi.org/10.1177/13694332211017995.
[31] Wang J, Dai Q, et al. Mechanical, durability, and microstructural properties of macro synthetic polypropylene (PP) fiber-reinforced rubber concrete. J Clean Prod 2019;234:1351–64. https://doi.org/10.1016/j.jclepro.2019.06.272.
[32] Sun J, Tang Y, et al. A multi-objective optimisation approach for activity excitation of waste glass mortar. J Mater Res Technol 2022. https://doi.org/10.1016/j.jmrt.2022.01.066.
[33] Xu H, Wang X-Y, et al. A 3D root system morphological and mechanical model based on L-Systems and its application to estimate the shear strength of root-soil composites. Soil Tillage Res 2021;212:105074. https://doi.org/10.1016/j.still.2021.105074.
[34] Xu J, Lan W, et al. Modeling of coupled transfer of water, heat and solute in saline loess considering sodium sulfate crystallization. Cold Reg Sci Technol 2021;189:103335. https://doi.org/10.1016/j.coldregions.2021.103335.
[35] Sun J, Wang X, et al. Multi-objective optimisation of a graphite-slag conductive composite applying a BAS-SVR based model. J Build Eng 2021;44:103223. https://doi.org/10.1016/j.jobe.2021.103223.
[36] Zhang W, Zhang R, et al. State-of-the-art review of soft computing applications in underground excavations. Geosci Front 2020;11(4):1095–106. https://doi.org/10.1016/j.gsf.2019.12.003.
[37] Wang P, Wang S-Z, et al. Cauliflower-shaped Bi_2O_3–ZnO heterojunction with superior sensing performance towards ethanol. J Alloys Compd 2021;854:157152. https://doi.org/10.1016/j.jallcom.2020.157152.
[38] Zhang W, Li H, et al. Application of deep learning algorithms in geotechnical engineering: a short critical review. Artif Intell Rev 2021;54(8):5633–73. https://doi.org/10.1007/s10462-021-09967-1.
[39] Huang Y, Zhang J, et al. Intelligent mixture design of steel fibre reinforced concrete using a support vector regression and firefly algorithm based multi-objective optimization model. Construct Build Mater 2020;260:120457.
[40] Singh V, Gu N, Wang X. A theoretical framework of a BIM-based multi-disciplinary collaboration platform. Autom ConStruct 2011;20(2):134–44.
[41] Xu S, Wang J, et al. Computer vision techniques in construction: a critical review. Arch Comput Methods Eng 2021;28(5):3383–97. https://doi.org/10.1007/s11831-020-09504-3.
[42] Sun J, Aslani F, et al. Fresh and mechanical behaviour of developed fibre-reinforced lightweight engineered cementitious composites for 3D concrete printing containing hollow glass microspheres. Ceram Int 2021. https://doi.org/10.1016/j.ceramint.2021.06.124.
[43] Al-Buriahi MS, Tonguc BT, et al. Investigation of barium borate glasses for radiation shielding applications. Appl Phys Mater Sci Process 2020;126(1):1–9.
[44] Al-Buriahi MS, Bakhsh EM, et al. Mechanical and radiation shielding properties of tellurite glasses doped with ZnO and NiO. Ceram Int 2020;46(11, Part B):19078–83. https://doi.org/10.1016/j.ceramint.2020.04.240.
[45] Al-Buriahi MS, Hegazy HH, et al. Effect of Sb_2O_3 addition on radiation attenuation properties of tellurite glasses containing V_2O_5 and Nb_2O_5. Appl Phys A 2021;127(2):106. https://doi.org/10.1007/s00339-020-04265-z.
[46] Hegazy HH, Al-Buriahi MS, et al. The effects of TeO_2 on polarizability, optical transmission, and photon/neutron attenuation properties of boro-zinc-tellurite glasses. J Inorg Organomet Polym Mater 2021;31(6):2331–8. https://doi.org/10.1007/s10904-021-01933-2.
[47] Al-Buriahi MS, Singh VP, et al. Mechanical features and radiation shielding properties of TeO_2–Ag_2O-WO_3 glasses. Ceram Int 2020;46(10, Part A):15464–72. https://doi.org/10.1016/j.ceramint.2020.03.091.
[48] Al-Buriahi MS, Alajerami YSM, et al. Effect of chromium oxide on the physical, optical, and radiation shielding properties of lead sodium borate glasses. J Non-Cryst Solids 2020;544:120171. https://doi.org/10.1016/j.jnoncrysol.2020.120171.

[49] Al-Buriahi MS, Somaily HH, et al. Polarizability, optical basicity, and photon attenuation properties of Ag_2o MoO_3 V_2OU TeO_2 glasses: the role of silver oxide. J Inorg Organomet Polym Mater 2020;31:1047–56.
[50] Olarinoye IO, Alomairy S, et al. Effect of Ag_2O/V_2O_5 substitution on the radiation shielding ability of tellurite glass system via XCOM approach and FLUKA simulations. Phys Scripta 2021;96(6):065308. https://doi.org/10.1088/1402-4896/abf26a.
[51] Alzahrani JS, Alothman MA, et al. Simulating the radiation shielding properties of TeO_2–Na_2O–TiO glass system using PHITS Monte Carlo code. Comput Mater Sci 2021;196:110566. https://doi.org/10.1016/j.commatsci.2021.110566.
[52] ASTM. Standard specification for standard sand. 2013. C778-13.
[53] Baykasoğlu A, Öztaş A, Özbay E. Prediction and multi-objective optimization of high-strength concrete parameters via soft computing approaches. Expert Syst Appl 2009;36(3):6145–55.
[54] Grygar D, Fabricius R. An efficient adjustment of genetic algorithm for pareto front determination. Transp Res Proc 2019;40:1335–42.
[55] Huang H, Huang M, et al. Experimental study of predamaged columns strengthened by HPFL and BSP under combined load cases. Struct Infrastruct Eng 2020:1–18. https://doi.org/10.1080/15732479.2020.1801768.
[56] Zhang G, Chen C, et al. Multi-objective optimisation design for GFRP tendon reinforced cemented soil. Construct Build Mater 2022;320:126297.
[57] Feng W, Wang Y, et al. Prediction of thermo-mechanical properties of rubber-modified recycled aggregate concrete. Construct Build Mater 2022;318:125970.
[58] Du Toit G, Kearsley EP, et al. Chemical and mechanical activation of hybrid fly ash cement. Adv Cement Res 2018;30(9):399–412.
[59] Chen F, Jin Z, et al. Relationship model between surface strain of concrete and expansion force of reinforcement rust. Sci Rep 2021;11(1):1–11. https://doi.org/10.1038/s41598-021-83376-w.
[60] Donatello S, Fernández-Jimenez A, Palomo A. Very high volume fly ash cements. Early age hydration study using Na_2SO_4 as an activator. J Am Ceram Soc 2013;96(3):900–6.
[61] Shi C, Day R. Early strength development and hydration of alkali-activated blast furnace slag/fly ash blends. Adv Cement Res 1999;11(4):189–96.
[62] Chen F-x, Zhong Y-c, et al. Non-uniform model of relationship between surface strain and rust expansion force of reinforced concrete. Sci Rep 2021;11(1):1–9. https://doi.org/10.21203/rs.3.rs-135397/v1.
[63] Shi C. Corrosion of glasses and expansion mechanism of concrete containing waste glasses as aggregates. J Mater Civ Eng 2009;21(10):529–34.
[64] Pascual AB, Tognonvi MT, Tagnit-Hamou A. Waste glass powder-based alkali-activated mortar. Int J Res Eng Technol 2014;3(13):32–6.
[65] Haha MB, Le Saout G, et al. Influence of activator type on hydration kinetics, hydrate assemblage and microstructural development of alkali activated blast-furnace slags. Cement Concr Res 2011;41(3):301–10.
[66] Shi C, Wu Y, et al. Alkali-aggregate reaction expansion of mortars containing glass powders. In: Tang M, Deng M, editors. Proceedings of the 12th international conference on alkali-aggregate reaction in concrete. Beijing: International Academic Publisher; 2004.
[67] Matos AM, Sousa-Coutinho J. Durability of mortar using waste glass powder as cement replacement. Construct Build Mater 2012;36:205–15.
[68] Sun J, Lin S, et al. The effect of graphite and slag on electrical and mechanical properties of electrically conductive cementitious composites. Construct Build Mater 2021;281:122606.
[69] Du H, Tan KH. Use of waste glass as sand in mortar: Part II–Alkali–silica reaction and mitigation methods. Cement Concr Compos 2013;35(1):118–26.